Bulletin of Engineering Geology and the Environment (2023) 82:67
https://doi.org/10.1007/s10064-023-03088-5

ORIGINAL PAPER

Impact of diagenesis and pore aspects on the petrophysical and elastic properties of carbonate rocks from southern Lebanon

Mohamed K. Salah[1] · H. T. Janjuhah[2] · Josep Sanjuan[3] · Elsa Maalouf[4]

Received: 3 December 2021 / Accepted: 28 January 2023 / Published online: 10 February 2023

Abstract

Carbonate rocks form under widely variable depositional settings and are susceptible to complicated diagenetic processes which influence their petrophysical and elastic properties. Understanding the controlling factors on these rock parameters is crucial for the interpretation of sonic logs and seismic reflection profiles. Herein, we collect a large number of carbonate rock samples exposed at southern Lebanon to examine the lithofacies, pore types, diagenetic processes, and their impact on the petrophysical and elastic properties. Collected samples belong to the Upper Cretaceous, Eocene, and Miocene limestone beds and are dominated by bioclastic packstone/wackestone from carbonate shelf deposits which are more susceptible to early diagenesis. Measured porosity is generally moderate to high and varies between 10 and 40%, with a pore system dominated by intraparticle, moldic, and vuggy pores. A small amount of porosity is represented by fractures and interparticle pores. Permeability is very low due to the dominance of isolated intraparticle porosity and small micropores. The measured density and the seismic wave velocities are low due to the moderate/high porosity and the presence of a significant (~ 17%) non-carbonate matrix. Many diagenetic features, such as micritization, cementation, compaction, and dissolution, impacted porosity and permeability differently (dependent on the pore throat size) and led also to the widely variable but generally low seismic wave velocities. The wide scatter observed in the porosity-velocity data cannot be explained solely by the microfacies, pore types, or mineralogy. Instead, we used effective medium theories to explain the variability of seismic velocities with porosity and the petrographic characteristics of the studied rocks. Modeling results show that, in addition to porosity, composition, rock texture, pore types, and the pore aspect ratios have significant impacts on the elastic properties of the studied samples which could explain the observed variations of seismic wave velocities at a given porosity. These findings are crucial for a better characterization of both onshore and offshore carbonate rocks which may host hydrocarbon, groundwater, and geothermal energy resources.

Keywords Lithofacies · Pore types · Diagenesis · Elastic properties · Carbonate rocks · Lebanon

Introduction

Carbonate rocks host significant hydrocarbon and groundwater reserves in wide regions of the world including China, Latin and Central America, and the Middle East (e.g., Nurmi and Standen 1997; Dürrast and Siegesmund 1999; Wenzhi et al. 2014; Jiang et al. 2014, 2015, 2018a, b and c; Thompson et al. 2015; Jin et al. 2017; Jiang 2022). Unlike sandstone reservoirs, exploration of carbonate reservoirs is complex because of intrinsic heterogeneities represented by variable composition, depositional settings, rock fabric, diversity of pore types, pore size, and pore shapes, which result from both syn- and post-depositional diagenetic processes (Kerans 1988; Loucks 1999, 2001; Akbar et al. 2001; Eberli et al. 2003; Soete et al. 2015; Salah et al. 2018, 2020a, b and c, 2023; Salih et al. 2020).

✉ Mohamed K. Salah
ms264@aub.edu.lb

[1] Department of Geology, American University of Beirut, Riad El Solh, Beirut 1107 2020, Lebanon

[2] Department of Geology, Shaheed Benazir Bhutto University, Sheringle, Upper Dir, Pakistan

[3] Departament de Dinàmica de La Terra I de L'Oceà, Institut de Recerca de La Biodiversitat-IRBio, Facultat de Ciències de La Terra, Universitat de Barcelona-UB, 08028 Barcelona, Catalonia, Spain

[4] Department of Chemical Engineering and Advanced Energy, American University of Beirut, Riad El Solh, Beirut 1107 2020, Lebanon

These prolonged processes affect the petrophysical and elastic properties, and in particular, the porosity-velocity (φ-V) relationship in carbonate rocks (Anselmetti and Eberli 1993; Brigaud et al. 2010; Neto et al. 2014). Therefore, carbonate rocks exhibit complicated φ-V correlation which affects the interpretation of sonic logs and seismic reflection profiles, compared to the simple inverse relationship characteristic for siliciclastic rocks.

Porosity is the main factor affecting seismic velocities in siliciclastic and carbonate rocks (Wyllie et al. 1958; Gardner et al. 1974; Raymer et al. 1980; Zolotukhin and Ursin 2000). However, observed differences in the elastic properties of carbonate rocks, in particular, cannot be explained only by observed porosity differences. Extensive research during the last few decades revealed that velocity variations in carbonate rocks are controlled additionally by other factors such as the pore geometry, pore structure, and the presence of fluids (Wang et al. 1991; Weger et al. 2009), the fluid pressure (Mavko et al. 2009), mineralogy, density, and pore types (Anselmetti and Eberli 1993, 2001; Kenter et al. 1997), rock texture and facies which are tightly related to depositional and diagenetic processes (Verwer et al. 2008; Ali et al. 2018). Moreover, studies of Kleipool et al. (2015) and Regnet et al. (2019) revealed that seismic velocities in carbonate rocks are generally affected by the amount and type of pore spaces, and specifically by the mineral composition, cementation, and the presence of microcracks.

Abd El-Aal et al. (2020), and Salah et al. (2020a) have previously conducted detailed petrophysical and elastic investigations on Jurassic and Cretaceous carbonates including dolostones which occur widely in geological records. Recent studies on the petrophysical and elastic properties of carbonate rocks from Lebanon (Salah et al. 2018, 2020a, b, c; 2023) revealed significant variations in the elastic properties at a given porosity. Although many factors were proposed to account for the observed disparities, further investigations are required to comprehend the complex φ-V relationship in the Lebanese carbonate rocks. In this study, we collect fifty samples from the upper Cretaceous and Tertiary carbonate rocks exposed at southern Lebanon to characterize their lithofacies, texture, pore types, and the diagenetic processes, and assess the impact of these parameters on the petrophysical and elastic properties. The selected rocks are rarely dolomitized and were formed mainly in carbonate platforms which are specifically susceptible to early diagenesis; hence adding further complexities of their petrophysical and elastic properties (Friedman 1964; Croizé et al. 2010). In particular, we examine the φ-V relationship by comparing the rock elastic properties to two effective medium models by incorporating different equivalent pore geometry (pore aspect ratio, AR) values to test the impact of AR on the φ-V relationship (Berryman 1980; Salih et al. 2020). The results of this study deepen our understanding of the different factors affecting the elastic properties of the studied limestones, which are critical for the interpretation of seismic reflection profiles and sonic logs acquired for subsurface fluid-bearing carbonate sequences in Lebanon.

Geologic setting

Lebanon is divided into three main geological entities following a general NNE-SSW trend; i.e., Mount Lebanon to the west of the central Bekaa Valley and the Anti-Lebanon in the east (Fig. 1A). The studied area is located to the southwest of Mount Lebanon near the coastal city of Sidon (Fig. 1B). The geology of the region is dominated by highly faulted marine carbonate sequences ranging in age from Late Cretaceous to Late Miocene (Walley 1998).

The upper Cretaceous/middle Eocene Sannine Formation represents the dominant lithological unit exposed in the area. It is a 200-m-thick succession composed of light grey featureless marls and limestones rich in calcareous nannoplankton and planktonic foraminifera, grading vertically to 200-m-thick marls alternated with nummulite-rich limestones and chert bands (Dubertret 1955). Müller et al. (2010) identified Danian to upper Paleocene rocks based on an assemblage of calcareous nannoplankton in Sidon (Paleogene nannofossil zones NP3–NP5). Janjuhah et al. (2021) recognized younger deposits in the same area (near the village of Qennarit) and correlated these deposits with the NP6 zone (uppermost Paleocene) of Martini (1970). Upper Eocene and Oligocene sedimentary sequences have not been detected in Sidon probably due to the tectonic uplift which affected the region during the second stage of the Syrian Arc deformational event (Walley 1998). This tectonic phase occurred in the late Eocene and continued up to the late Oligocene leading to a long-lasting erosional period in which no sedimentation prevailed until the early Neogene (Dubertret 1955). Neogene deposits in the area are represented by Miocene carbonate conglomerates overlain by marine marls and reefal limestone beds near Maghdoucheh and south of Choualiq (Dubertret 1945; Hawie et al. 2014).

According to Müller et al. (2010), the Miocene rocks in Sidon range in age from Burdigalian to Langhian (Neogene nannofossil zones NN3–NN5). Slightly older and younger ages have recently been reported in Maghdoucheh by Janjuhah et al. (2021) based on microfossil records. These authors indicated that the Miocene sedimentary sequence at Maghdoucheh is correlated with the Neogene nannoplanckton zones NN2–NN6 which range in age from lower Burdigalian to Serravalian. Miocene beds were deposited in a shallowing-upward sequence from open deep shelf to shallow internal platform environments related to the middle Miocene marine transgression that postdates the major uplift of the Mount of Lebanon (Müller et al. 2010; Janjuhah et al. 2021). Another erosional phase occurred during the late Neogene due to the drop of the sea level, which

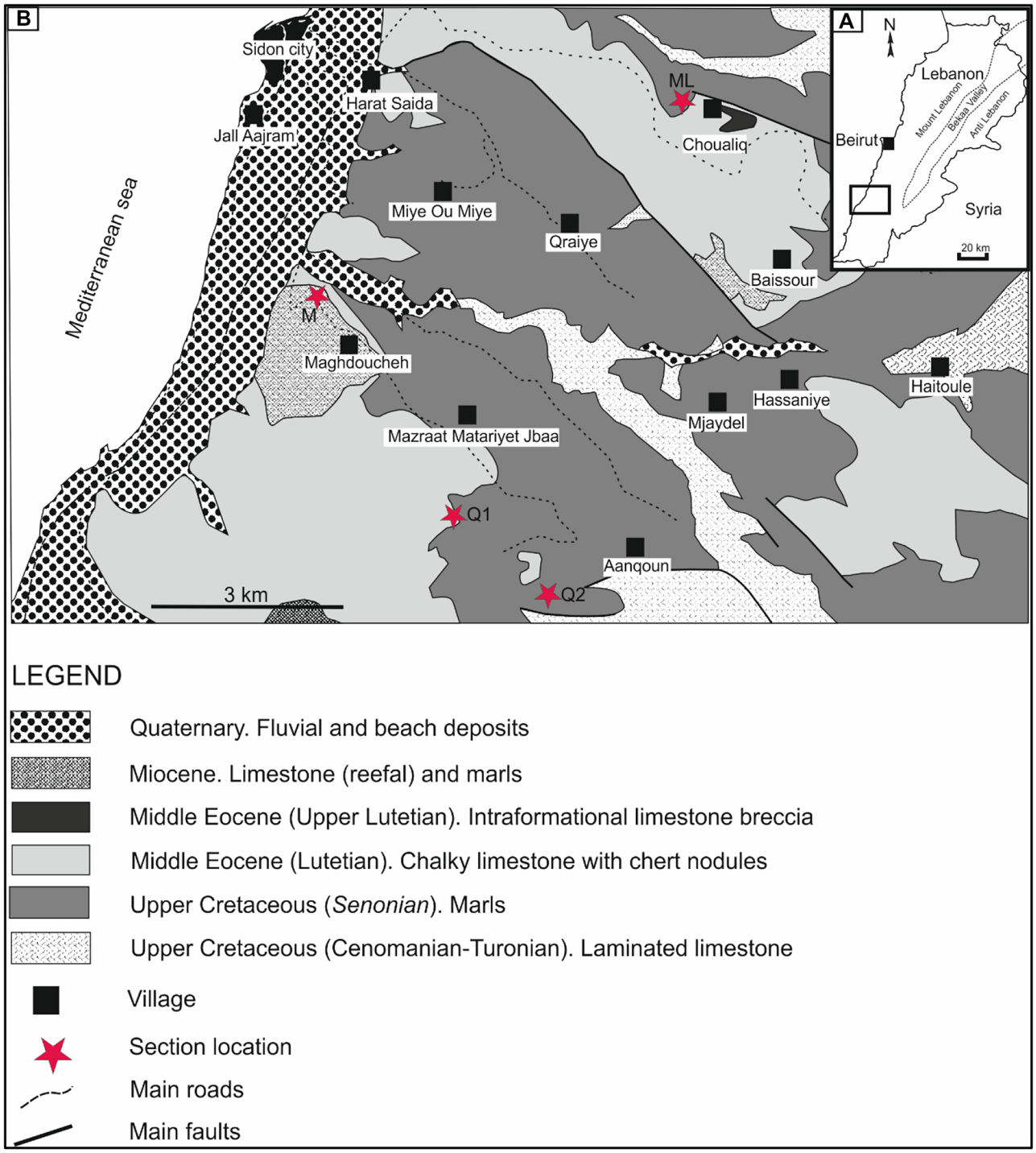

Fig. 1 Geological map of the studied area at southern Lebanon (modified from Dubertret, 1945, after Salah et al. 2023). Red stars indicate the locations of the four studied stratigraphic sections (M = Maghdoucheh, Q1 = Quennarit-1, Q2 = Quennarit-2, and ML = Choualiq)

eroded the previous carbonate deposits and led to the simultaneous sedimentation of fluviatile terraces and coastal beach sands (BouDagher-Fadel and Clark 2006).

The upper Cretaceous, Paleocene and Miocene marine carbonate sequences in this area are represented mainly by marls, limestones (sometimes chalky) alternating in some locations with chert bands (Janjuhah et al. 2021). These rocks experienced many diagenetic processes such as micritization, cementation, compaction, neomorphism, and little dolomitization which influenced their porosity, and

permeability. According to Janjuhah et al. (2021), porosity detected in the studied rocks is mainly secondary with moldic, vuggy, fenestral, intraparticle, and fractures as dominant pore types.

Materials and methods

Four stratigraphic sections were sampled from the exposed upper Cretaceous, middle Eocene and Miocene carbonate rocks at Maghdoucheh, Qennarit and Choualiq in southern Lebanon; only 3 km to the south of Sidon (Fig. 1). The base coordinates of the four stratigraphic sections (one in Maghdoucheh, two in Qennarit, and one in Choualiq) are shown in Fig. 2 and specified in Janjuhah et al. (2021). Fifty cylindrical cores of one-inch-diameter were collected from the hard carbonate beds outcropping at the four aforementioned sections. Collected samples and drilled cores were used to study the microfacies, textural features, diagenetic processes, petrophysical and elastic properties. Twenty-five 30-µm-thick thin sections were prepared at the CoreLab of Texas (USA) to study the rock microfacies and diagenetic processes. These samples were also investigated by the SEM (MIRA 3LMU Scanning Electron Microscopy) at the Central Research Science Laboratory (CRSL) of the American University of Beirut (AUB). Small bits from the twenty-five samples were crushed and powdered for the x-ray diffraction (XRD) analysis to examine the mineralogy of the studied rocks. The advanced BRUKER D8 x-ray diffractometer at the CRSL at AUB was used to conduct the XRD analysis. Then, the acid insoluble residue (AIR) test was conducted to calculate the proportion of non-carbonate components in the studied rocks (Blatt 1992). A small mass of about 2–4 g of the dry powdered rock was dissolved in 10% hot HCl for 24 h to digest the carbonate fraction completely, then followed by the calculation of the AIR percentage.

Thin sections were examined using transmitted light microscopy to determine the pore types and quantify their percentage. On average, 32 photos were taken for each thin section to cover the entire thin section area. These microphotographs were stacked on top of one another to provide a combined view and to clearly characterize the pore types using the point counting approach. Porosity and permeability were measured using the porosity–permeability (poro-perm) measuring system of

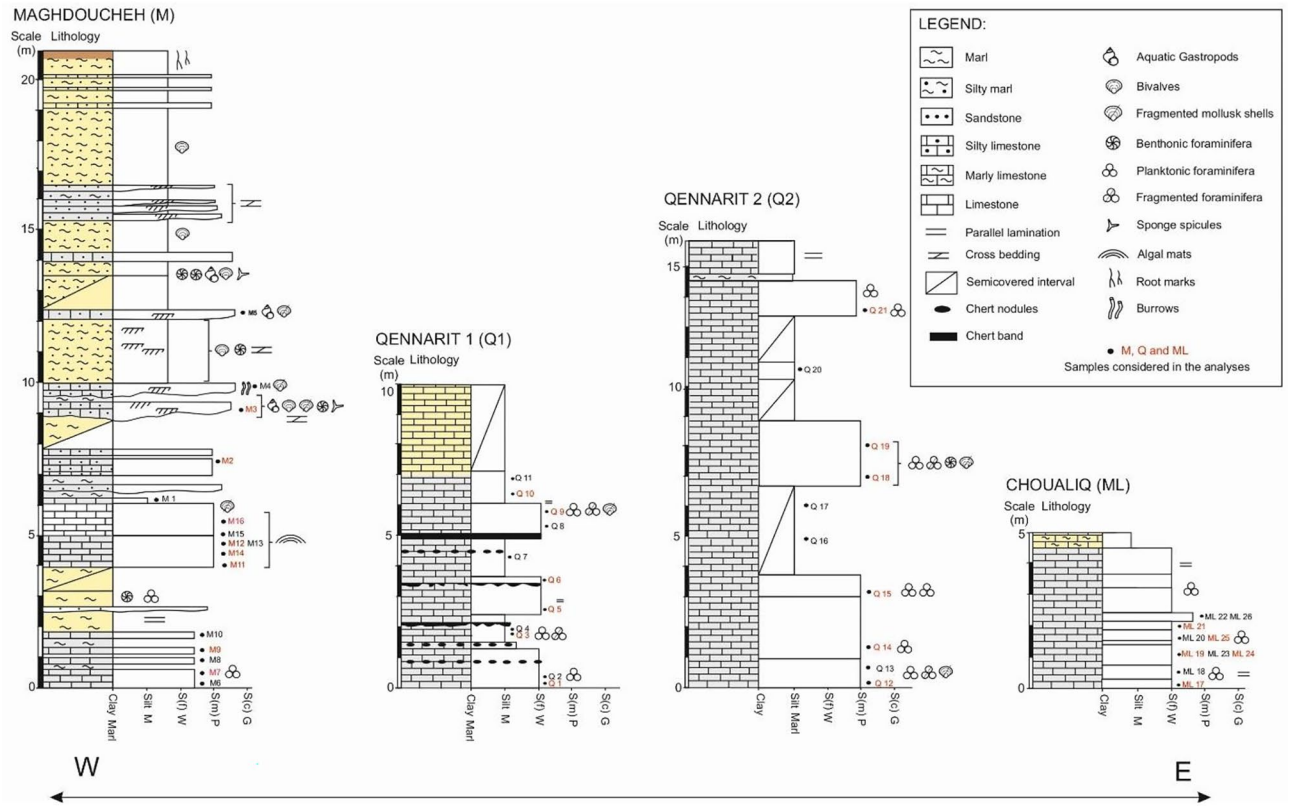

Fig. 2 Stratigraphic logs of the studied four sections: Magdoucheh (Miocene), Qennarit-1 (Eocene), Qennarit-2 (late Cretaceous), and Choualiq (late Cretaceous). Orange capital letters—M (Magdoucheh section), Q (Qennarit- Sects. 1 and 2), and ML (Choualiq section)—represent the stratigraphic position of the samples used for lithofacies analysis and petrophysical measurements (modified from Salah et al. 2023)

the Core Laboratories known as CMS-300™. Porosity (φ) is obtained by dividing the volume of pores by the bulk volume of the core sample. The measured nitrogen permeability—calculated using Darcy's law—was rectified for the effect of gas slippage (Jones 1972) as described in Salah et al. (2020c). The bulk and grain densities (ρ_b, and ρ_g) were computed from the dry mass of the core sample divided by the bulk and grain volumes, respectively.

Acoustic velocities were measured on dry samples using ultrasonic techniques. Core sample tips were trimmed and loaded in the acoustic velocity device which is equipped with a 1 MHz acoustic transmitter and receiver. A pressure of 100 psi was applied to hold a sample in place. The device records the travel time (t) across the sample which is then converted to wave velocity (V) using $V=d/t$ where d is the length of the core sample. Further details on the Corelab acoustic measuring system are given in Salah et al. (2018). Dynamic elastic moduli (the Young's modulus (E), the bulk modulus (κ), and the shear modulus (μ)) and the Poisson's ratio (ν) were calculated from the density and acoustic wave velocities (e.g., Telford et al. 1990; Kearey et al. 2002). Table 1 lists the obtained petrophysical and elastic properties while Table 2 summarizes the lithofacies, pore types, and textural parameters of the studied rocks.

The measured velocities are then compared to two effective medium theories namely the differential effective medium (DEM) model and the self-consistent approximation (SCA). The DEM models help in identifying the parameters that control the φ-V relationship such as the rock matrix, mineral inclusion, porosity, and the shape and size of pores. The DEM theory estimates effective elastic moduli (bulk modulus and Poisson's ratio) of a two-phase mixture by incrementally adding inclusions of one phase (phase 2) to the host rock (phase 1) until phase 2 reaches a desired concentration x_2. The effective bulk modulus (K_{DEM}) and Poisson's ratio (ν_{DEM}) are given by Berryman (1980) as:

$$(1-x)\frac{d}{dx}\left[K_{DEM}(x)\right] = \left(K_2 - K_{DEM}\right)P_{DEM_2}(x) \quad (1)$$

$$(1-x)\frac{d}{dx}\left[\nu_{DEM}(x)\right] = \left(\nu_2 - \nu_{DEM}\right)Q_{DEM_2}(x) \quad (2)$$

where x is the volumetric concentration of the inclusion phase (phase 2) with bulk modulus K_2 and Poisson ratio ν_2. The inclusion phase could be either a mineral or a pore. P and Q are geometric factors depending on the inclusion shape and aspect ratio, and subscript DEM_2 indicates that P and Q are calculated for an inclusion of material 2 in a background medium with elastic properties K_{DEM} and ν_{DEM}. The calculation of the geometric factors P and Q are detailed in Appendix A. At each increment, the calculated effective elastic properties are used as properties of the matrix material in the next increment. In the first iteration, $K_{DEM}(x=0)=K_1$ and $\nu_{DEM}(x=0)=\nu_1$ where K_1 and ν_1 are the elastic properties of the initial host rock (i.e., phase 1). Rocks are often composed of more than two phases; in that case, the mixture's effective elastic properties are calculated in several steps by adding each phase successively. However, the order in which inclusions are added does not necessarily describe the real evolution of the rock.

The SCA model estimates the effective stiffness tensor of an N-phase mixture using.

$$\sum_{i=1}^{N} x_i\left(K_i - K_{SCA}\right)P_{SCA_i} = 0 \quad (3)$$

$$\sum_{i=1}^{N} x_i\left(\nu_i - \nu_{SCA}\right)Q_{SCA_i} = 0 \quad (4)$$

where K_{SCA} and ν_{SCA} are the effective bulk modulus and Poisson's ratio; x_i is the volumetric concentration of inclusion i with bulk modulus K_i and Poisson's ratio ν_i. The inclusion phase is either a mineral or a pore. P and Q are geometric factors that depend on the inclusion shape and aspect ratio, and subscript SCA_i indicates that P and Q are calculated for an inclusion of material i in a background medium with effective elastic properties K_{SCA} and ν_{SCA}. The calculation of the geometric factors P and Q are detailed in Appendix A.

Results

Lithofacies

The base of Magdoucheh section is composed of a 4 m layer of marl alternated with thin intervals of limestone (Fig. 2). Limestone beds display packstone textures enriched in intraclasts and foraminifera (samples M7 and M9). Overlying deposits are represented by 15 m of yellowish silty marls alternating with cross-stratified microfossils-rich sandy limestones showing erosive bases (Fig. 2). Different lithofacies have been detected in the collected samples from Qennarit, Maghdoucheh, and Choualiq sections (Fig. 3A–H). Thin limestone beds (5 to 30 cm in thickness) show grain-supported fabrics, i.e., packstone (samples M2 (Fig. 3C) and M3) and boundstone (bindstone) textures (samples M11 (Fig. 3F), M12, M14, and M16). Carbonate grains in packstone microfacies are mainly intraclasts and bioclasts including fragments of ostracods, echinoids, mollusks, and benthic foraminifera (sample M2, Fig. 3C). Porosity under the microscope varies widely in the investigated boundstone samples being consistent with the measured values which range from 10.6% (sample M16) to 39.7% (sample M11).

Qennarit−1 section (samples Q1−Q11) is represented by 10-m-thick limestone strata alternated with several chert bands (Fig. 2). Metric limestone beds show parallel

Table 1 Measured and calculated petrophysical and elastic parameters of the studied core samples

Sec	#	φ, (%)	ρ_b (g/cm^3)	ρ_g (g/cm^3)	AIR (%)	K (mD)	Vp (m/s)	Vs (m/s)	μ (10^{10} Pa)	κ (10^{10} Pa)	E (10^{10} Pa)	ν
Maghdoucheh Samples	M2	25.2	2.02	2.69	17.23	0.49	2755	1653	0.551	0.796	1.343	0.22
	M3	35.6	1.75	2.69	20.00	0.60	1901	1174	0.241	0.310	0.574	0.19
	M7	12.8	2.36	2.70	11.53	<0.01	4769	2731	1.759	3.018	4.419	0.26
	M9	18.6	2.18	2.70	12.33	0.03	3718	2202	1.057	1.602	2.599	0.23
	M11	39.7	1.59	2.68	10.50	14.4	2528	1263	0.254	0.680	0.679	0.33
	M12	12.2	2.37	2.70	5.50	0.10	3622	2187	1.132	1.594	2.747	0.21
	M14	28.6	1.89	2.67	4.00	0.89	3222	1702	0.548	1.232	1.431	0.31
	M16	10.6	2.38	2.65	17.55	<0.01	4628	2706	1.746	2.779	4.331	0.24
Qennarit Samples	Q1	29.7	1.89	2.61	31.85	0.01	2383	1526	0.439	0.485	1.012	0.15
	Q3	36.1	1.68	2.55	40.35	0.027	2408	1443	0.349	0.507	0.853	0.22
	Q5	31.8	1.77	2.59	29.75	0.055	2538	1599	0.454	0.538	1.062	0.17
	Q6	30.6	1.87	2.61	26.30	0.02	2337	1518	0.432	0.448	0.980	0.13
	Q9	36.8	1.72	2.57	36.50	0.048	2475	1597	0.438	0.468	1.002	0.14
	Q10	36.8	1.57	2.55	35.25	0.058	2294	1385	0.302	0.425	0.733	0.21
	Q12	32.5	1.81	2.70	5.00	0.106	3900	2300	0.957	1.475	2.360	0.23
	Q14	34.7	1.77	2.71	4.00	0.211	3710	2174	0.836	1.322	2.072	0.24
	Q15	30.7	1.87	2.71	4.20	0.21	3984	2298	0.989	1.655	2.475	0.25
	Q18	13.7	2.34	2.71	7.20	0.02	5096	2811	1.854	3.619	4.750	0.28
	Q19	31.2	1.83	2.70	6.43	0.139	3593	2178	0.870	1.208	2.106	0.21
	Q21	11.4	2.44	2.72	7.20	<0.01	5286	2915	2.071	4.049	5.308	0.28
Choualiq Samples	Ml17	34.7	1.72	2.64	9.87	0.150	2790	1506	0.390	0.818	1.009	0.29
	Ml19	31.7	1.79	2.65	9.90	0.065	2668	1423	0.363	0.792	0.945	0.30
	Ml21	17.8	1.96	2.30	32.70	<0.01	3616	2266	1.007	1.222	2.370	0.18
	Ml24	18.5	1.95	2.31	8.85	<0.01	3607	2252	0.991	1.220	2.340	0.18
	Ml25	21.4	1.88	2.39	31.45	<0.01	3655	2266	0.966	1.226	2.296	0.19
Average		26.54	1.94	2.62	17.02	0.93	3339	1963	0.84	1.34	2.07	0.22

φ porosity, ρ_b bulk density, ρ_g grain density, *AIR* the acid insoluble residue, K gas permeability, Vp primary wave velocity, Vs secondary wave velocity, μ shear modulus, κ bulk modulus, E Young's modulus, and ν Poisson's ratio

Table 2 Lithofacies, pore types, and other textural parameters as identified under the microscope for the studied samples

Sec	#	Lithofacies	Pore types (%) Md/Ipa/Ipe/Fr/Vg*	Roundness and sphericity	Sorting	Grain size	Dominant carbonate grains
Maghdoucheh Samples	M2	Packstone	40/35/5/0/20	Low	Poor	<200 µm	Intraclasts and benthic forams
	M3	Packstone	25/50/0/5/20	Low	Poor	<150 µm	Bioclasts and benthic forams
	M7	Packstone	50/30/0/5/15	Low	Poor	<200 µm	Intraclasts
	M9	Packstone	40/20/5/0/35	Low	Poor	<200 µm	Planktonic forams
	M11	Boundstone	20/40/5/10/25	x	x	x	Red algae
	M12	Boundstone	50/30/0/0/20	x	x	x	Red algae
	M14	Boundstone	15/25/0/5/55	x	x	x	Red algae
	M16	Boundstone	40/55/0/0/5	x	x	x	Red algae
Qennarit Samples	Q1	Wackstone	30/40/5/0/25	Low	Moderate	<200 µm	Planktonic forams
	Q3	Wackstone	35/45/0/5/15	Low	Poor	<250 µm	Intraclasts
	Q5	Wackstone	25/40/5/5/25	Low	Poor	<200 µm	Bioclasts
	Q6	Wackestone	30/50/0/0/20	Low	Poor	<200 µm	Bioclasts
	Q9	Wackstone	35/45/0/5/15	Low	Poor	<200 µm	Bioclasts
	Q10	Packstone	30/40/5/5/20	Low	Poor	<200 µm	Planktonic forams
	Q12	Packstone	35/45/5/5/10	Low	Moderate	<300 µm	Planktonic forams and other bioclasts
	Q14	Packstone	35/40/0/5/20	Low	Moderate	<300 µm	Planktonic forams and other bioclasts
	Q15	Packstone	30/50/0/0/20	Low	Poor	<200 µm	Planktonic forams
	Q18	Packstone	60/20/5/0/15	Low	Poor	<200 µm	Planktonic forams
	Q19	Packstone	30/45/5/0/20	Low	Poor	<200 µm	Planktonic forams
	Q21	Packstone	40/45/0/0/15	Low	Moderate	<200 µm	Planktonic forams
Choualiq Samples	Ml17	Wackstone	45/50/0/0/5	Low	Poor	<100 µm	Planktonic forams
	Ml19	Wackstone	60/35/0/0/5	Low	Poor	<200 µm	Planktonic forams
	Ml21	Wackstone	45/50/0/0/5	Low	Poor	<100 µm	Bioclasts
	Ml24	Wackstone	60/35/5/0/0	Low	Poor	<100 µm	Planktonic forams
	Ml25	Wackstone	50/40/0/5/5	Low	Poor	<100 µm	Bioclasts

*Pore types are as follows: *Md* Moldic, *Ipa* Intraparticle, *Ipe* Interparticle, *Fr* Fracture, and *Vg* Vuggy

lamination and matrix-supported textures, i.e. wackestone (sample Q3, Fig. 3D). Skeletons of *Globigerina sp.* represent the dominant bioclasts in this section, and are poorly preserved and broken in some samples (sample Q5, Fig. 3H). The Qennarit−2 section (samples Q12−Q17) is composed of a sequence of 15-m-thick limestone beds displaying grain supported textures (packstone) rich in planktonic foraminifera, other bioclasts, and fecal pellets. Skeletons of foraminifera are empty in several samples (e.g. sample Q19, Fig. 3B). In general, samples of the Qennarit sections exhibit high porosities of 30% or even higher. Only two samples, i.e., Q18 and Q21 have moderate porosities of 11.4 and 13.7%, respectively (Table 1).

The Choualiq section (samples ML1−25) is built of five-m-thick homogeneous light grey chalky limestone with micrite-supported textures, i.e. wackestone (Fig. 2 and Table 2). Dominant carbonate grains include empty skeletons of planktonic foraminifera and intraclasts (sample ML17, Fig. 3G). The measured porosity is moderate to high where it varies between 17.8 and 34.7% (Table 1).

In total, five standard microfacies (SMF) types are recognized in the studied limestone beds. These SMF are distinguished based on the identification and interpretation scheme of carbonate rocks proposed by Flügel (2010).

SMF 2: Microbioclastic peloidal calcisiltite

SMF 2 has been identified in some samples of Qennarit−2 section. According to Flügel (2010), this microfacies forms under open marine shelf environment, and the abundant carbonate clasts in this microfacies are exemplified by well-preserved shells of foraminifera, bioclasts, and fecal pellets.

SMF 3: Pelagic lime mudstone and wackestone with planktonic microfossils

SMF 3 occurs in some samples from Qennarit−1 section (Q1, Q3, Q6 and Q10), and in all samples of the Choualiq section (ML1-26). Bioclasts are represented by well-preserved skeletons of planktonic foraminifera. According to

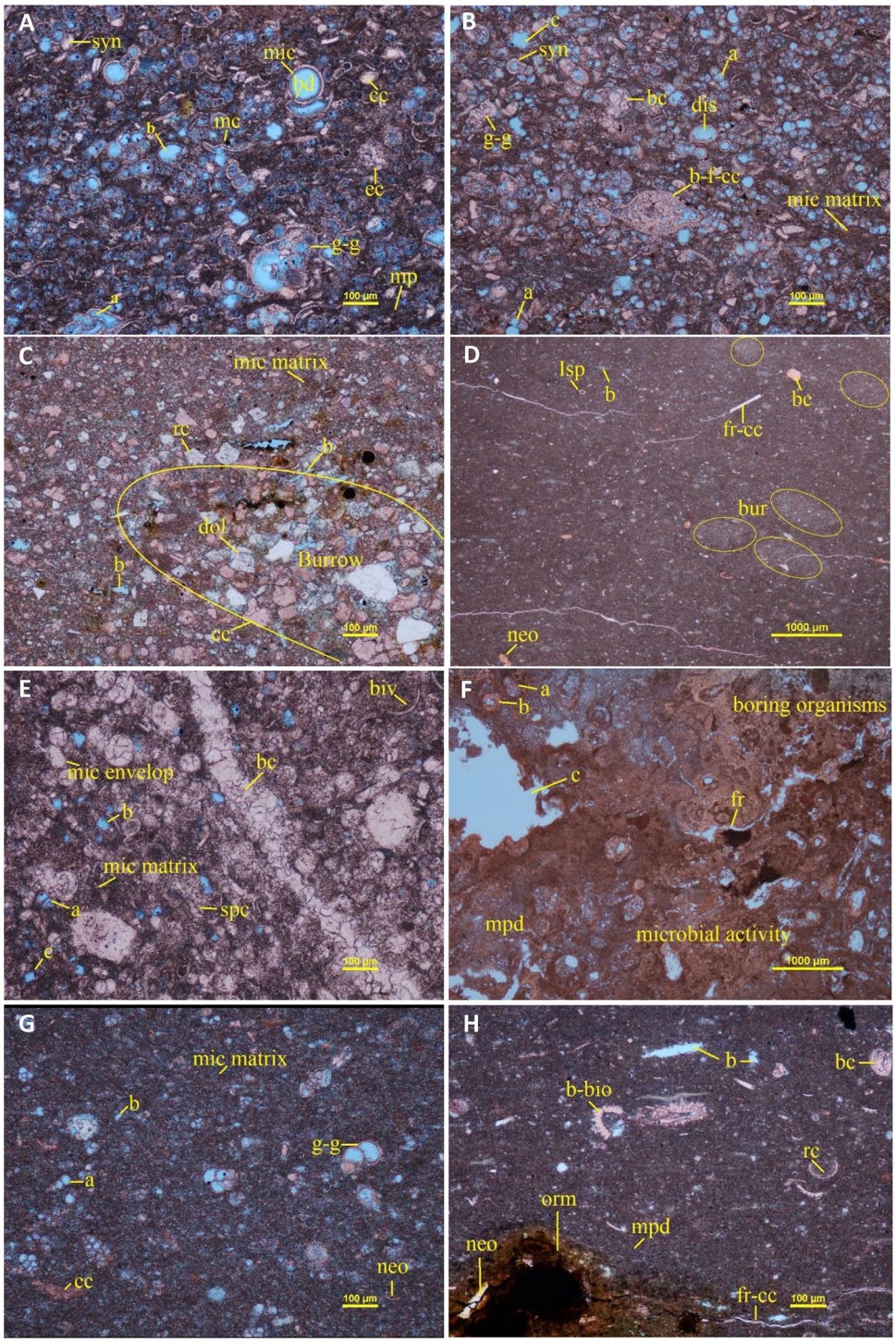

Flügel (2010), SMF 3 is formed in open deep carbonate shelf environemnts.

SMF 10: Bioclastic packstone and wackestone with abraded and worn skeletal grains

SMF 10 is detected in the samples of Qennarit−2 section and in some samples from Qennarit−1 section (Q5 and Q9). Bioclasts in this microfacies are dominated by worn and/or well-preserved skeletons of foraminifera. Benthic foraminifera and fragments of mollusks occur also but in minor amounts. SMF 10 forms in an open sea carbonate shelf or open lagoons and is common in mid-ramp regions (Flügel 2010).

◂**Fig. 3** Petrographic photos showing carbonate textures and porosities from the limestone samples at Magdoucheh (M) Qennarit (Q) and Choualiq (ML). **A** Sample Q12: a-intraparticle porosity, b-moldic porosity, mic-micrite envelop, syn-syntaxtial overgrowth cement, cc-calcite cement, ec-equant calcite cement, bd-bladed cement, g-g-grain to grain compaction, mp-micropores, mc-mechanical compaction; **B** Sample Q19: a-intraparticle porosity, b-moldic pore, f-foraminifera, cc- internal chamber filled with calcite cement, bc- blocky cement, dis-dissolution, syn-syntaxtial overgrowth cement, g-g: grain-to-grain contact, c-vuggy pores, mic-micrite matrix; **C** Sample M2: rc-recrystallization, b-moldic pores, dol-dolomite, cc-calcium calcite, mic matrix-micrite matrix; **D** Sample Q3: bc-blocky cement, fr-cc fracture filled with calcite cement, neo-neomorphism, bur- burrow, b-moldic pores, Isp-isopachous cement; **E** Sample Q21: bc-blocky cement, mic envelop-micrite envelop, biv-bivalve, bc-blocky cement, spc-equant spar cement, a-intraparticle, b-moldic, c-vuggy pores; **F** Sample M11: a-intraparticle, b-moldic, c-vuggy, mpd-micropores dominated section, boring organisms, microbial activity, fr-fracture; **G** Sample Ml17: a-intraparticle, b-moldic pores, g-g: grain to grain contact, neo-neomorphism, cc-calcite cement, mic matrix- micrite matrix dominated section; **H** Sample Q5: fr-cc fracture filled with calcite cement, orm-organic rich mud, neo-neomorphism, mpd-microporous dominated section, rc-recrystallization, b-bio-broken fragments of bioclasts, bc-blocky cement, and b-moldic pores

SMF 18: Packstone with abundant foraminifera

SMF 18 has been observed in the Miocene deposits at Maghdoucheh. The packstone textures, the presence of fragmented bioclasts, and traction structures indicate highly energetic depositional conditions. Paleoenvironmental characteristics deduced from the recovered microfossil assemblage (dominated by benthic foraminifera and mollusks) are in line with the microfacies interpretation, i.e. the fauna thrived in shallow and agitated conditions (Janjuhah et al. 2021). According to Flügel (2010), SMF 18 occurs in bars and channels subjected to tidal currents in shallow bays with open circulation or in back reef settings.

SMF 21: Fenestral boundstone, mudstones, and packstones with porostromate microstructures

SMF 21 is detected in the Miocene deposits at Maghdoucheh (samples M11, M13, M14, and M16). This microfacies forms in intertidal shallow internal platforms (Flügel 2010).

Pore types and diagenetic processes

The pore system of the studied samples is dominated by isolated intraparticle pores (Figs. 3 and 4). Inspection of thin sections (Fig. 3A–B, and E) indicated that the moldic and intraparticle pores are dominant. Based on the classification of Choquette and Pray (1970), the detected pore types, in order of predominance, are intraparticle, moldic, vuggy, fracture, and interparticle pores (Figs. 3, 4A–D, 5 and Table 2).

The studied carbonate rocks have undergone various diagenetic processes represented by micritization, cementation, dissolution, replacement, compaction (both physical and chemical), fracturing, and filling (Fig. 6). As revealed in Fig. 3, the micrite envelope is the first observed diagenetic process. The skeletal components underwent moderate to complete grain micritization (Fig. 3A–C, and E). In addition, indicators of boring organisms and high degrees of microbial activity are present. The framework is mainly composed of predominantly clotted fabrics (Fig. 3F).

Multiple generations of calcite cement are observed in the studied rocks (Figs. 3 and 4). Fine- to medium-sized blocky cement is detected in the packstone microfacies with completely filled pore spaces, some vugs and molds (Figs. 3B, E and 4B). The blocky cement extends up to 90 μm in length in some samples (Figs. 3E and 4B). A syntaxtial overgrowth cement is seen in the skeletons of foraminifera which displays a partially well-developed outer layer of micrite envelopes (Fig. 3A–B). Occasionally, the observed micrite envelopes represent subtle and faint laminations, which are marked in places by muddy lamina (Fig. 3A). Other forms of cements such as bladed (Fig. 3A), blocky (Figs. 3B and 4B), and isopachous (Fig. 3D) are observed in some samples. Euhedral dolomite from the pore-filling medium was only observed in sample M2 (Fig. 3C). All the different types of calcite cements largely occlude the intraparticle, moldic, and vuggy pores (Figs. 3A–C, E and 4A–E).

Intensive dissolution is observed in secondary porosity formed during the early-late stages of diagenesis (Figs. 3A–C and 4A–B). Early-stage dissolution resulted in the partial degradation of grains forming intraparticle porosity (Fig. 4A), while fabric- to non-fabric-selective dissolution dominates the late stages resulting in moldic and vuggy porosities (Figs. 3A–B and 4C–D).

The grain-to-grain contacts, the distribution pattern of different grains, and the fractures observed in the present study (Fig. 3B–F) are all related to the overburden pressure. Frequently, globular skeletons of planktonic foraminifera display grain-to-grain contacts (Fig. 3A, E). It should be noted that the packstone microfacies is the dominant lithophase which exhibits mechanical compaction (Figs. 3A, C, E and 4C–E). This mechanical compaction is manifested by the fracturing, breakage, and the tight packing of grains.

Calcite recrystallization of skeletal grains is transformed into calcite spars that resulted in aggradation neomorphism (Fig. 3D). Dolomite crystals are rare in the studied sections and were detected only in one sample (M2 in Fig. 3C), as non-ferroan, very fine to fine crystals.

Quantitative analysis of thin sections

Packstone is the dominantly observed texture representing 50% of the studied thin sections; the wackstone and

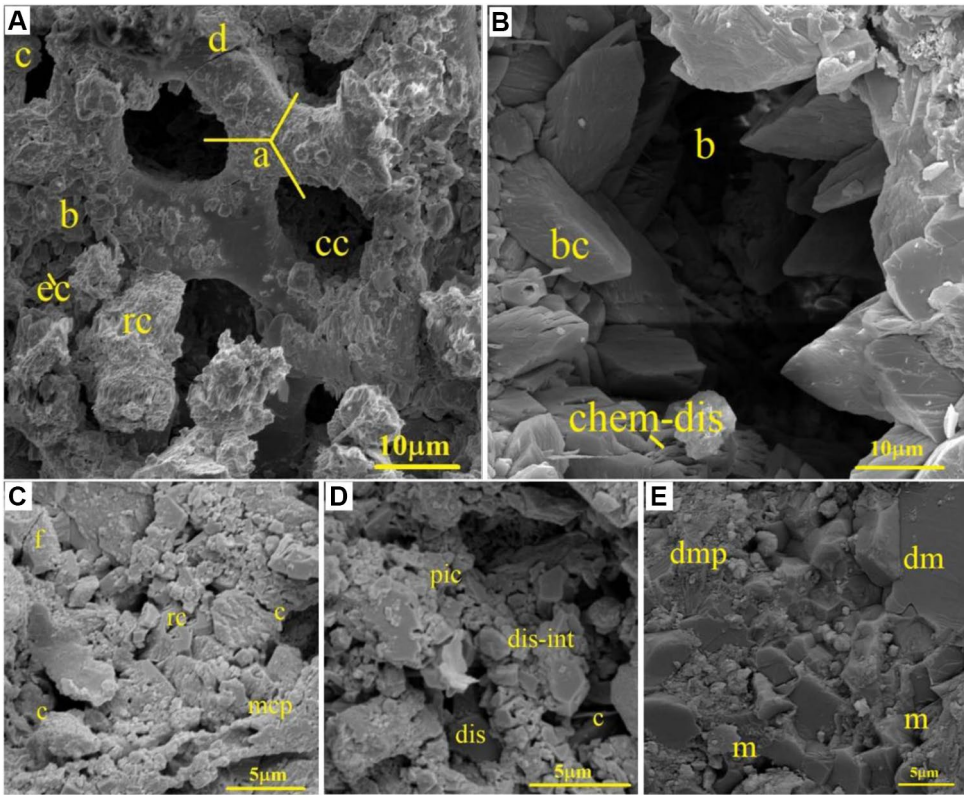

Fig. 4 SEM images showing the pore types from the limestone samples at Magdoucheh (M) Qennarit (Q) and Choualiq (ML). **A** Sample M2: a—intraparticle porosity, b—moldic porosity, c—vuggy porosity, d—fracture, ec-equant calcite cement, rc-recrystallization, and cc-calcite cement; **B** Sample Q12: b—moldic porosity, bc-blocky cement, chem-dis–chemical dissolution by fluids reacting with calcite cements altering the morphology of micrite particles; **C** Sample M-14: c—vuggy porosity, mcp-micrite particles glued together to form bigger grains having negative impact on porosity and permeability, rc-recrystallization, f-fracture; **D** Sample Ml25: c—vuggy porosity, pic-poorly interconnected micrite particles, dis-int–dissolution processes altering the micrite particles resulting in interlocking, dis-dissolution; **E** Sample Ml25: m—isolated micropores, dmp-dense closely packed micrite particles, dm-dissolved micrite particles due to dissolution

boundstone constitute the remaining 50% (Fig. 5A). Grains constitute 33% of the rock, while the matrix and cement represent 32% and 25%, respectively. The remaining 10% are represented by visible porosity (Fig. 5B). The qualitative analysis of the visible porosity revealed five different pore types (Fig. 5C). The intraparticle porosity is dominant representing almost 40% of the detected pore types followed by 38% moldic pores, 17% vuggy pores, 3% fracture porosity, and lastly 2% interparticle pores (Fig. 5C and Table 2).

Petrophysical and elastic properties

The measured porosity is generally moderate to high where it varies from 10.6% to 39.7% with an average of 26.5% (Table 1). Samples of Maghdoucheh and Choualiq have moderate to high porosities, while those of Qennarit sections have predominantly high porosities. The bulk density is generally low with an average of 1.94 g/cm^3. The grain density is also small (average 2.62 g/cm^3), which is lower than the typical value of pure calcite at 2.76 g/cm^3. The AIR varies largely from a minimum of 4% in nearly pure limestones (e.g., samples M14 and Q14) to a maximum value of 40.35% in marly samples with an overall average of 17.02% (Table 1). Although the studied rocks have moderate to high porosities, they possess very low to low permeabilities. Six out of the twenty-five, samples have permeabilities < 0.01 mD (Table 1). The permeability of other samples is also low and does not exceed 15 mD (Table 1). The poro-perm cross plot (Fig. 7A) shows that five samples from Qennarit-1 section (Q1, Q3, Q6, Q9, and Q10) possess a permeability lower than 0.1 mD although their porosities are greater than 29%. On the other hand, the porosity-bulk density cross plot (Fig. 7B) shows the small bulk density of the studied rocks.

Three samples (ML21, ML24, and ML25) appear below the main porosity-bulk density trend (Fig. 7B). The presence of isolated pores may explain the low bulk density and/or the low porosity of these samples. Table 1 and Fig. 7C indicate that some of the studied carbonate rocks contain significant non-carbonate fraction, which influences their petrophysical and elastic properties. The majority of the samples display a

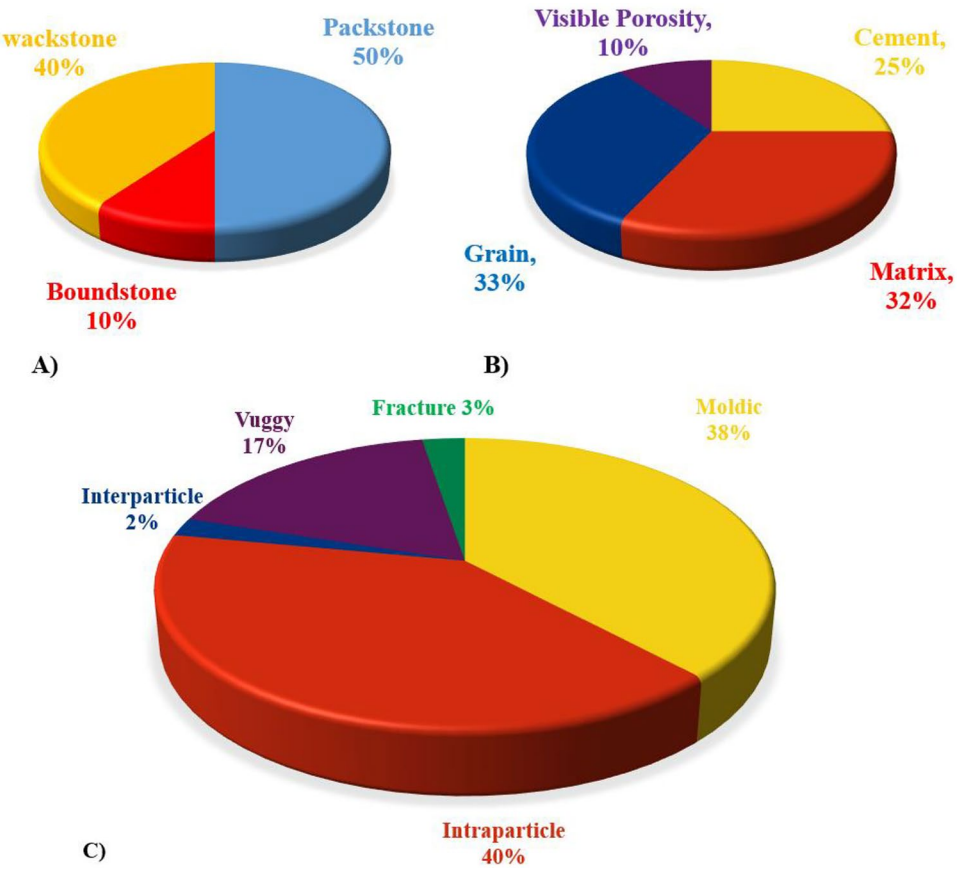

Fig. 5 Graphics showing **A** the quantitative distribution of lithofacies, **B** rock components and textures, and **C** the different pore types in the studied samples

positive correlation between porosity and the AIR (Fig. 7C), revealing that the non-carbonate fraction enhances porosity. Some samples, i.e., M11, M14, Q12, Q14, Q15, Q19, ML17, and ML19 exhibit low AIR but high porosities, which can be explained by the development of secondary 'diagenetic' porosity in otherwise carbonate rocks of low primary porosity.

The acoustic wave velocities are generally low to moderate with average Vp and Vs values of 3340 and 1963 m/s, respectively (Table 1). These average velocities give a small Vp/Vs ratio of 1.70 which is consistent with the small but widely variable ν (the Poisson's ratio varies from 0.13 to 0.33 with a small average of 0.22). In general, samples having the highest velocities (e.g., Q21, Q18, and M7), have low/moderate porosities. On the other hand, highly-porous rocks such as samples M3, M11, and Q10 exhibit low velocities. The average rigidity, bulk, and young's moduli are 0.84, 1.34, and 2.07×10^{10} Pa, respectively (Table 1).

Discussion

Depositional and diagenetic history

The studied rocks bear many features that reflect their depositional and diagentic history and that greatly impact on their petrophysical properties. Skeletons of bioclasts observed in some samples under the microscope (sample Q5, Fig. 3H) are poorly preserved and broken indicating syn-depositional reworking. Several samples (e.g., sample Q19, Fig. 3B) comprise empty shells of foraminifera, thus enhancing porosity which is consistent with the measured value of this sample at 31% (Table 1). Samples of the Choualiq section contain empty skeletons of planktonic foraminifera and intraclasts which enhance the porosity significantly (sample ML17, Fig. 3G). These observations are confirmed by the measured porosity which varies between 17.8 and 34.7% (Table 1). On the other hand, samples Q18 and Q21 are dominated by isolated moldic and intraparticle pores (Fig. 3E and Table 2) which do not contribute significantly to the effective porosity and permeability. Hence, these two samples have porosities of 13.7 and 11.4%, respectively, and very low permeabilities of less than 0.02 mD (Table 1).

Digenesis plays a critical role in controlling the reservoir quality (e.g., Jiang et al. 2014; Grundtner et al. 2016; Janjuhah et al. 2018). The petrographic characteristics of the studied samples show that the observed diagenetic processes overprinted the pore size distribution, and greatly influenced the original pore-throat structure.

Brett and Brookfield (1984) described syn-sedimentary micritization as the occurrence of micritic bio-erosion fringes that extend from the grain's surface to its center.

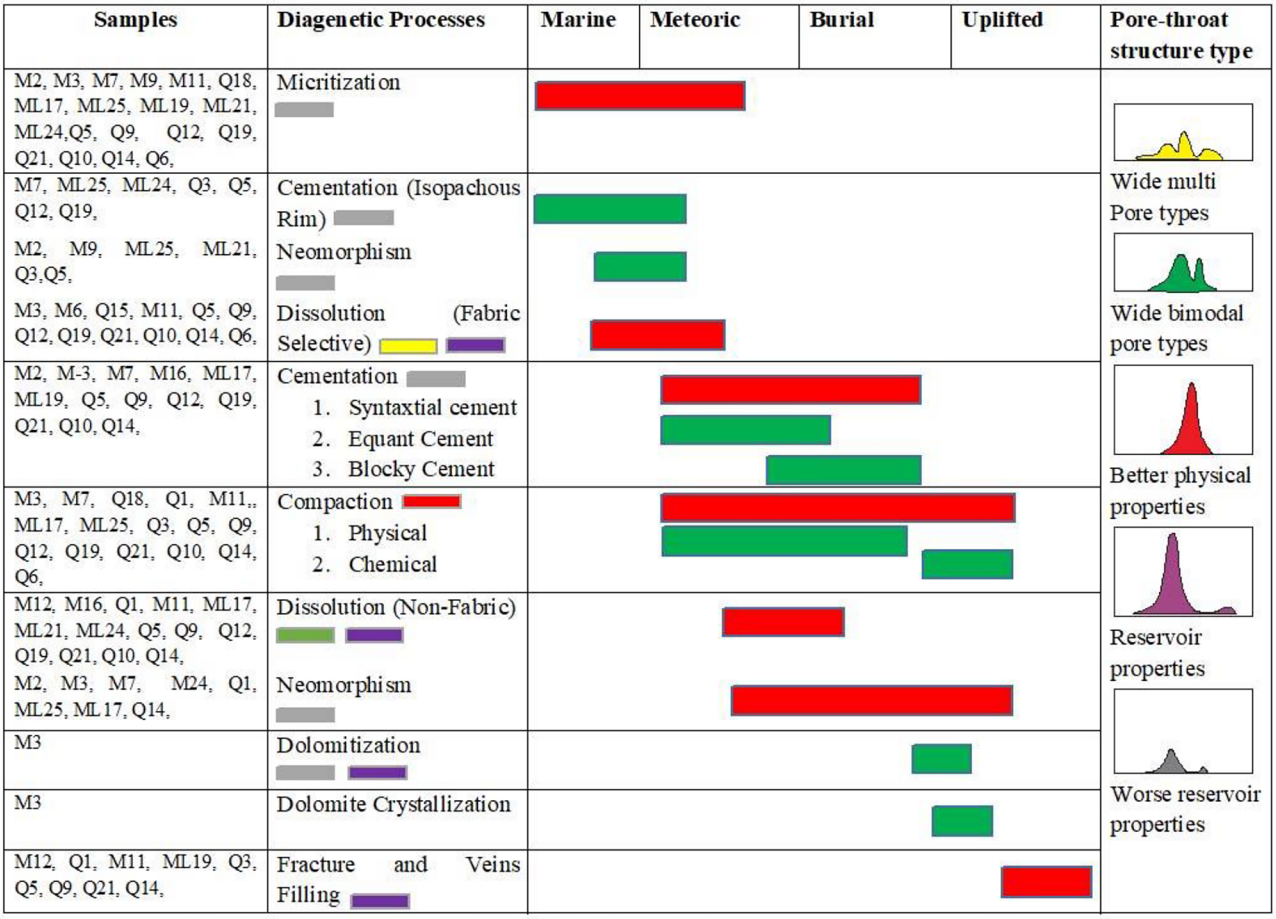

Fig. 6 The paragenetic sequence of the different diagenetic processes observed in the studied samples at Magdoucheh (M) Qennarit (Q) and Choualiq (ML). The last column displays the pore throat structures

Micrite envelopes demonstrate concurrent modification and deposition (Janjuhah et al. 2017; Ge et al. 2020; Tomašových et al. 2022). The presence of the micrite envelopes confirms the early stage of micritization (Fig. 3A–C). Numerous researchers (e.g., Tucker and Wright 2009; Morad et al. 2018; Janjuhah and Alansari 2020; and Grundtner et al. 2016) found also that when sediment and water interact in low-energy, slow-sedimentation environments, micritization is the first diagenetic process. Moreover, the presence of the micrite matrix indicates another late stage of micritization (Fig. 3B).

According to Hajikazemi et al. (2010); van Smeerdijk Hood and Wallace (2012) and Fallah-Bagtash et al. (2020), the diagenetic blocky calcite cement precipitates in marine environments. Syntaxial overgrowth cements are a rather early diagenetic feature, predating both mechanical compaction and some pore-lining cements (Oluwadebi et al. 2018; Busch et al. 2022). Thus, syntaxial overgrowths are associated with the primary distribution of echinoderm material and with specific, more open-grained sedimentary textures (Alsuwaidi et al. 2021). Turbid syntaxial overgrowths have been linked with phreatic marine environments, while clear syntaxial overgrowths have been associated with shallow burial (Flügel 2010; Swei and Tucker 2012; Hussein and Abd El-Rahman 2020). According to Flügel (2012) and Jin et al. (2020), the transition from non-luminescence to syntaxial overgrowths is commonly associated with the declining of pore fluids during progressive burial.

The term "dissolution" refers to the leaching of metastable bioclasts as a result of the presence of meteoric water (Budd 2002; Lambert et al. 2006; Tucker and Wright 2009; Janjuhah and Alansari 2020). Early dissolution of aragonite may have occurred in seawater or under shallow burial depths (Varkouhi and Jaques Ribeiro 2021), whereas compaction is induced mainly by overburden stresses, and sometimes by variations in the underground temperature causing high pore pressure and subsequent alteration of pores due

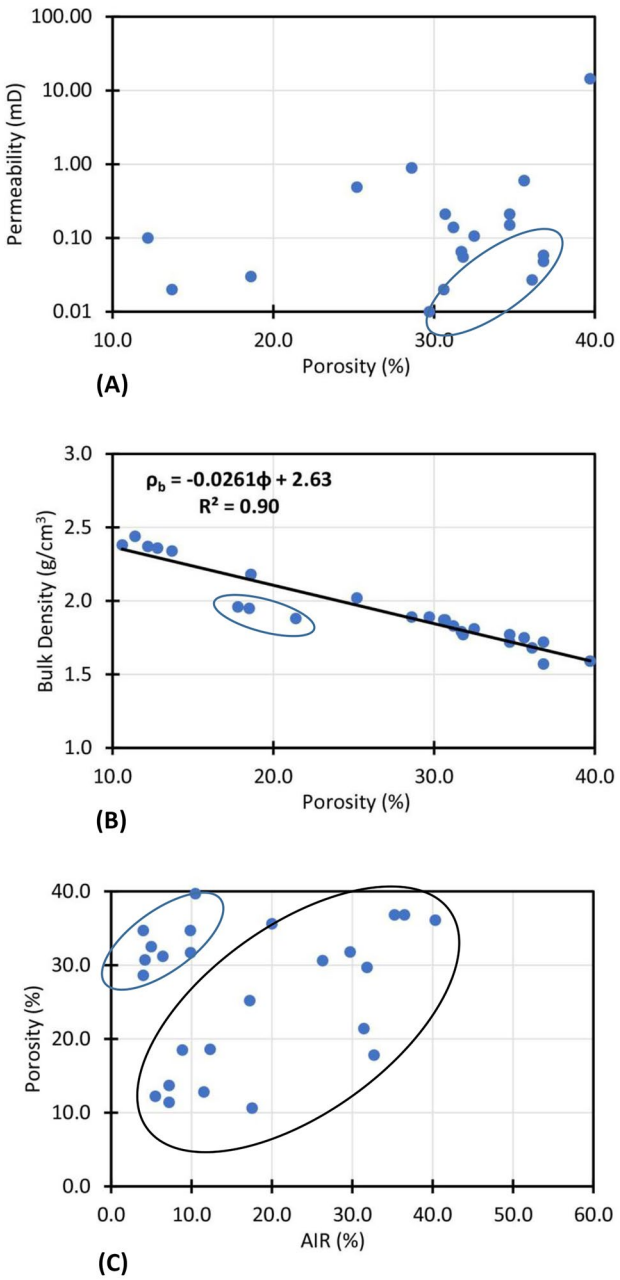

Fig. 7 Cross plots of porosity versus permeability (**A**), bulk density (**B**), and the AIR percentage (**C**). Note the positive trend of the poro-perm relationship (**A**). Three samples deviate clearly from the inverse φ-ρ_b trend in **B** due to the presence of isolated pores (refer to later sections for more details)

to chemical reactions between the water and the rock grains (Janjuhah and Alansari 2020; Pei et al. 2020).

The presence of calcite with an extremely high magnesium content in the shells of skeletal components enhances the process of recrystallization (Amel et al. 2015). Skeletal grains such as shells of foraminifera and echinoderms exhibit aggrading neomorphism with coated micrite envelopes suggesting sub-aerial diagenesis (Rosales and Pérez-Garcia 2010). Marls at Maghdoucheh are rich in planktonic foraminifera such as *Globigerina* sp., and *Orbulina universa* (Janjuhah et al. 2021). A rich microfossil assemblage including several taxa of benthic foraminifera and mollusks was extracted from these deposits as reported by Janjuhah et al. (2021). The pore system detected in the carbonate rocks of southern Lebanon is dominated by isolated vugs and intraparticle pores (Figs. 3 and 4), which resulted from the leaching of skeletal grains of planktonic and benthonic foraminifera, resulting in the partial or complete destruction of the original rock fabric (Janjuhah et al. 2021). This selective dissolution occurred rapidly after burial and was facilitated by the main composition of the skeletons, which consists of either aragonite or a high-magnesium calcite, both of which are extremely water-soluble (Hashim and Kaczmarek 2019; Janjuhah et al. 2019a; Babasafari et al. 2020; Kershaw et al. 2021). Janjuhah et al. (2021) also showed that calcite cement filled empty spaces in these carbonate rocks.

Impact of diagenesis and pore types on the petrophysical properties

The poro-perm relationship is valuable in formation evaluation and reservoir characterization (Ghadami et al. 2015; Janjuhah et al. 2019a). It is worth noting that micritization is the primary diagenetic process that affects reservoir quality by destroying the internal structure of the grains and reducing porosity. Micritization reduces the porosity of carbonate rocks by filling the pore throat radius or grain size with micrite (Xi et al. 2015). Paganoni et al. (2016) reported that micritization and compaction significantly decrease porosity in carbonate rocks.

The majority of the studied samples are characterized by very low permeability (Table 1 and Fig. 7A). Based on the observed diagenetic processes, leaching affected the bioclastic grains and created predominantly moldic and intraparticle pores that are isolated in nature. Furthermore, samples of Choualiq section are dominated by micritic textures with skeletons of planktonic foraminifera. These skeletons are heavily leached, hence, forming small isolated moldic pores, which are not normally considered as standard macropores and do not contribute to fluid flow (Ehrenberg and Walderhaug 2015; Janjuhah et al. 2019b). The presence of micropores, the closer packing of grains which resulted from the mechanical compaction (Figs. 3A, C and 4C–D), and the poor pore connectivity (Figs. 3D and 4D–E) are other reasons that explain the observed low permeability. The micropores are associated with intense micritization, cementation, and compaction as detected in the petrographic study and the SEM imaging. Hence, the diagenetic processes have different impacts on porosity and permeability because they affect the pore space differently and the inter-connection between the pores.

Modeling and the controlling factors of φ-V relationships

It has been observed that the different pore types encountered in carbonate rocks induce diverse velocities at a given porosity (e.g., Sun et al. 2006). In general, rocks with moldic or intraparticle pores have usually high initial velocities with small increases at increasing pressures. On the φ-V plots, samples possessing moldic pores plot above the regression line; those with micropores, micro-molds and framework pores plot below; whereas samples with dominantly vuggy pores plot around the best fit line (Eberli et al. 2003; Soete et al. 2015). Velocity is generally low in rocks with preliminarily higher percentage of microporosity which increases at higher pressures but never reaches the velocity of very rigid rocks with the same porosity.

The measured seismic wave velocities and the resulting ν values are lower than expected for carbonate rocks (e.g., Weger et al. 2009). Moreover, the φ-V data reveal wide velocity variations at a given porosity (Table 1; Fig. 8A). Although the φ-V and density-velocity plots (Fig. 8A, B) display, respectively, inverse and proportional relationships, we observe a wide scatter in the data points resulting in low R^2 values. For example, samples Q6 and Q15 have similar porosities of 30.6 and 30.7%, respectively; however, sample Q15 has a Vp that is 70% greater than that of Q6. Considering that both samples have the same pore types (Table 2), the different velocity values are likely induced by variations in pore stiffness (Regnet et al. 2015; Janjuhah et al. 2019b) or pore shapes. Similarly, samples M3 and Q14 exhibit close porosities of 35.6 and 34.7%, but significantly different Vp values of 1901 and 3710 m/s, respectively, even though their pore types are similar (Table 2). Similar observations are also detected for Vs data. Samples M7 and Q18 have more than 50% moldic pores and plot well above the regression line (Fig. 8A). In addition, samples Q12, Q14, Q15, Q19, and Q21 have significant proportions of intraparticle and moldic pores and plot above the regression line. Samples having significant amount of vuggy pores such as M2, M3, M9, M12, Q1, Q5, and Q6 plot below the regression line (Fig. 8A). Although samples M9, ML19, ML24, and ML25 are dominated by moldic pores, they plot well below the regression line. Additionally, velocities vary also widely at a given density (Fig. 8B). These variations might be caused by a blend of parameters including rock texture, pore types, pore connectivity, and pore aspect ratios. Diagenetic processes may open new pores, reduce the size of, or even close, existing pores which affect the measured seismic velocities significantly. Furthermore, the elastic properties of the rocks are calculated via ultrasonic measurements which are affected by the distribution of pores and their types within the samples with respect to the specific location of transducers across the core whenever the rocks are heterogeneous (e.g., Martínez-Martínez et al. 2012).

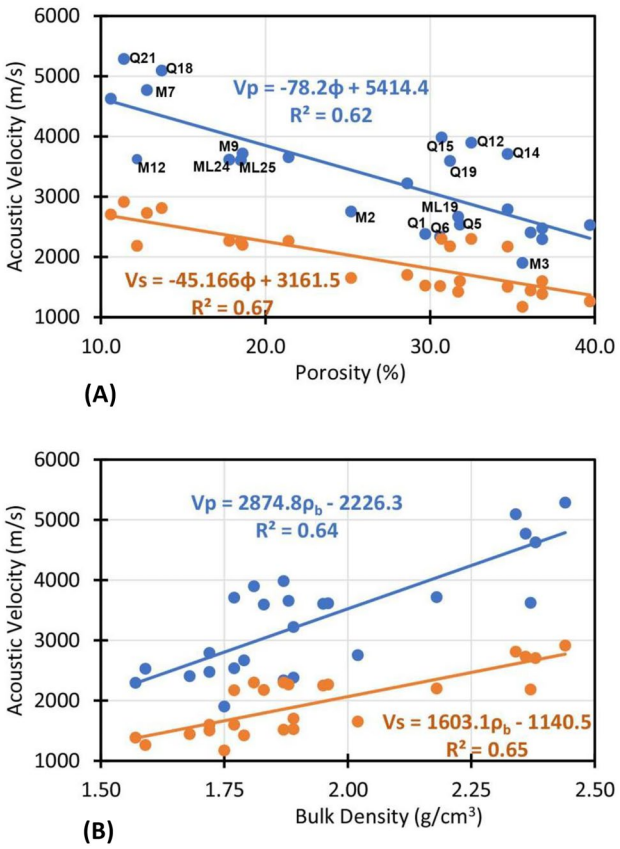

Fig. 8 Graphics of the acoustic wave velocities versus porosity (**A**), and bulk density (**B**). Note the wide scatter observed in the φ-V and density-velocity plots (see text for details)

In order to characterize the factors controlling the observed scatter in the φ-V relationships (Fig. 8A), the porosity-velocity data are plotted and classified (color coded) according to lithofacies (Fig. 9), dominant pore type (Fig. 10) and the percentage of the non-carbonate component (Fig. 11). Figure 9 shows that most of the packstone textures plot above, the wackstone textures below, whereas boundstones plot close to, or below, the regression line, respectively. Nonetheless, samples having the same lithofacies still exhibit wide ranges of velocities at a given porosity. Thus, no clear separation is obtained based on the lithofacies type, being consistent with the results of Salih et al. (2020). Similarly, Fig. 10 exhibits a wide scatter among samples having similar pore types. Samples dominated by intraparticle pores are equally distributed above and below the regression line; those dominated by moldic pores are below, and one sample dominated by vuggy pores is located very close/below the regression line. When the porosity-velocity data are replotted according to the percentage of the non-carbonate fraction (Fig. 11), no clear separation is evident and there is also a wide scatter in the samples especially those with less than 10% AIR. However, samples having higher AIR ratios tend to have lower velocities at a given porosity.

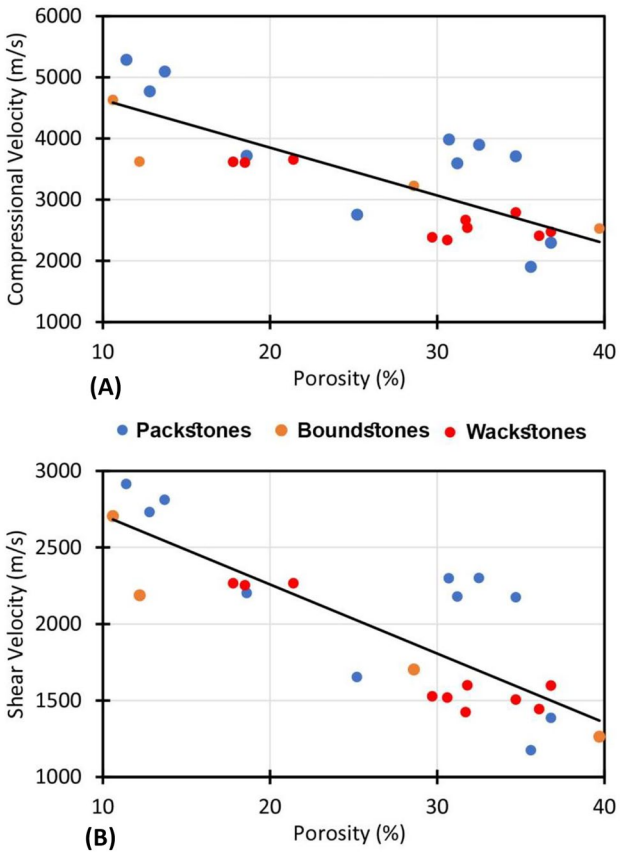

Fig. 9 Graphics of the Vp (**A**) and Vs (**B**) as a function porosity with the data points classified based on the lithofacies

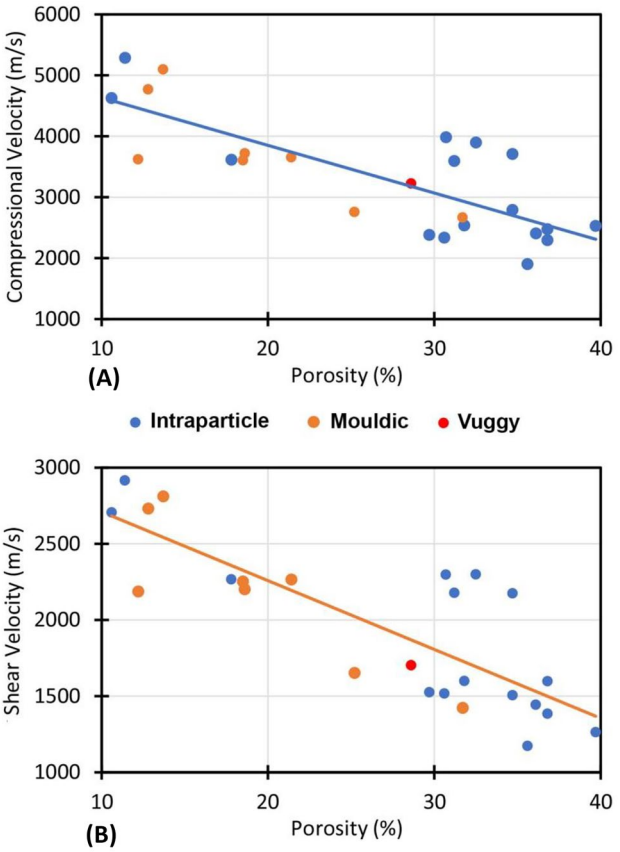

Fig. 10 Graphics of the Vp (**A**) and Vs (**B**) as a function porosity with the data points classified based on the dominant pore type

The XRD analysis is used to identify the mineralogy of the studied rocks and its effect on the observed velocities. Figure 12 indicates that all samples are composed predominantly of calcite, which represents more than 90% of the matrix in at least half of the samples. However, traces of quartz are detected in samples Q1–Q10 from Qennarit (Fig. 12A); higher percentages are detected in some samples from Maghdoucheh (e.g., M2, M3, M7, M11, and M16) and in sample ML25 from Choualiq (Fig. 12B). The presence of quartz is confirmed by the higher AIR values of these samples (Table 1). Dolomite is detected only in sample M2 (Fig. 12B) from the Maghdoucheh locality. Figure 11 shows that most of the samples containing quartz and dolomite display lower velocities at a given porosity. However, some samples exhibit high velocities which indicates that mineralogy cannot solely explain the variability of the φ-V data. Therefore, the effect of mineralogy on the observed scatter in the φ-V plots is minor; a fact that was also documented by other researchers (e.g., Christensen and Szymanski 1991; Salih et al. 2020).

A given pore type is usually characterized by a specific pore shape which influences the pore resistance to compression (pore stiffness). Spherical pores resist compression and induce high bulk moduli and high compressional velocities (Salih et al. 2020). In order to assess the impact of pore shapes on the measured velocity, we modeled the φ-V relationship using the DEM and the SCA methods as explained in the "Materials and methods" section. The DEM and SCA modeling methods yield the elastic properties of the medium for pores of varying aspect ratio, which is compared with the measured data. Figure 13 shows the φ-V data, whereas Fig. 14 shows the compressional and shear impedances against porosity superimposed by the curves obtained from the DEM and SEM modeling assuming different pore aspect ratios. The analysis is performed assuming a single matrix composed of a mixture of calcite and quartz (dominant minerals in all samples) with the values of $K_m = 68.8$ GPa, $\mu_m = 34.2$ GPa, $\rho_m = 2.698$ g/cm^3. The pores are assumed to be air-filled where $K_a = 142$ kPa and $\rho_a = 0.001$ g/cm^3. Ellipsoidal inclusions are assumed for the pores with aspect ratios of 0.04, 0.08, 0.12, 0.17, and 0.2. In the case of the SCA method, the aspect ratio of the background matrix is assumed to be 0.1; hence giving similar results to the ones obtained using the DEM method.

The results of the -V modeling reveal that the scatter of the velocity data around the linear trend of Fig. 8 results from the

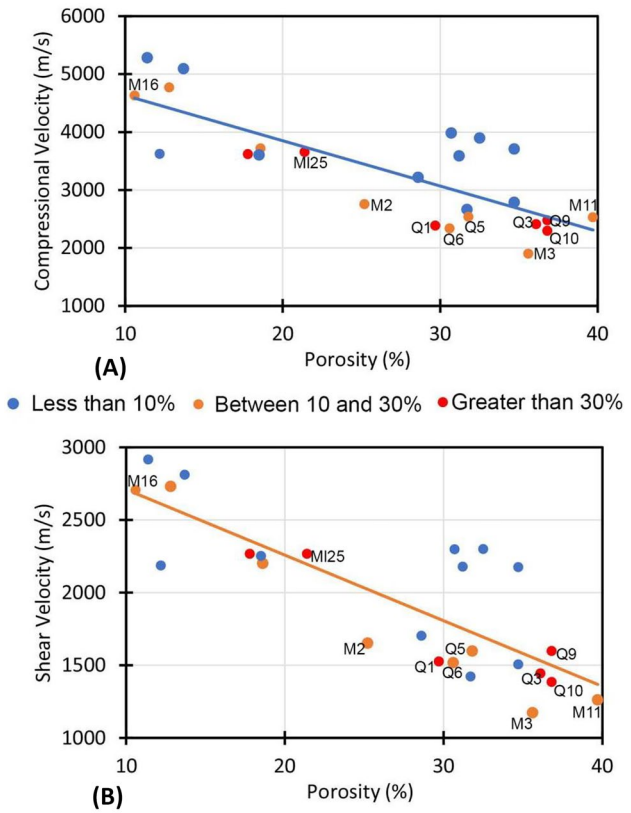

Fig. 11 Graphics of the Vp (**A**) and Vs (**B**) as a function porosity with the data points classified based on the acid insoluble residue (AIR) fraction

non-spherical pores and the varying aspect ratios present in the samples. For example, at a porosity of 30.6%, varying the AR from 0.2 to 0.08 causes a 70% decrease in Vp. Furthermore, Fig. 14 indicates an improved grouping of the impedance data with respect to the pore AR based on the pore type. It was noted that varying the matrix type does not significantly change the curves which are mainly controlled by the pore AR and the porosity as revealed by the DEM and SCA models.

The present analysis and the modeling results indicate that the φ-V relationship in carbonate rocks is controlled by many factors including porosity itself, the non-carbonate fraction, lithofacies, the pore types, pore stiffness, pore shapes (pore aspect ratios), and the different diagenetic processes. These results are crucial for a better quantitative analysis of seismic data and sonic logs, which in turn can reduce risks associated with hydrocarbon exploration and drilling programs in carbonate strata (Dvorkin et al. 2014). The large variations observed in the compressional and shear impedances (Fig. 14), point to possible significant changes in reflection coefficients, and thus vertical and spatial variations in the reservoir interval (Mavko et al. 2009; Salih et al. 2020). These variations may be further complicated by the existence of fluids in the pore spaces of the studied carbonate rocks.

Conclusions

Carbonate rocks exposed near Sidon, southern Lebanon were selected to study the effects of microfacies, pore types, mineralogy, and diagenetic processes on the petrophysical and elastic properties. Packstone and wackstone textures are the dominant microfacies with only few boundstone textures found in Maghdoucheh samples. The petrographic study and the SEM imaging revealed moderate to high porosity that is represented mainly by intraparticle and moldic pores. Few samples have significant proportions of vuggy porosity. Fracture and interparticle pores were also observed in the studied rocks but both represent a very low percentage of the observed porosity. The studied rocks have more or less homogeneous mineralogy dominated by calcite with minor amounts of quartz, and an average fraction of 17% of non-carbonate components.

Measured porosity and permeability vary significantly. Although the measured porosity is generally moderate to high, permeability is very low due to intense micritization and the small size of the resulting pores as well as the poor pore connectivity. The bulk and grain densities are generally low due to the high porosity and the presence of some clastic components as revealed by the AIR and XRD analyses. The observed seismic wave velocities and Poisson's ratios are lower than the characteristic ranges of carbonate rocks. The φ-V relationship shows a very wide scatter and large velocity variations at a given porosity (both at moderate and high porosities).

We investigated the different parameters controlling the observed scatter in the φ-V relationship including microfacies, pore types, and mineralogy. Detailed analyses revealed that either rock textures, pore types, or mineralogy do not, on their own, explain the observed scatter in the φ-V relationship. Modeling of the φ-V data using DEM and SCA methods revealed that pore shapes, besides the aforementioned parameters, account for the scatter of the seismic velocity and impedance data at a given porosity. The improved fit between the effective medium models with the φ-impedance data compared to the φ-V data indicates that parameters such as rock texture, along with pore types and shapes influence the petrophysical and elastic characteristics of the carbonate rocks, and can better explain the observed velocity variations at a given porosity.

The present results revealed that factors such as lithological composition, rock texture, pore types, pore shapes, and the different diagenetic processes combine together to produce characteristic pore stiffness and pore shapes; hence specific seismic velocities and elastic properties at a given porosity. Therefore, we propose that variations in the different proportions of pore types, most of which is diagenetic, pore shapes, and the resulting pore geometry

account for the observed variations in the petrophysical characteristics and the wide scatter in the φ-V relationship. This inference points to the importance of integrating the petrophysical and elastic properties of rocks while exploring and evaluating subsurface carbonate reservoirs. Moreover, the present study on the porosity and velocity of the carbonate rocks in Lebanon allows for better interpretation of seismic and logging measurements which are needed to locate potential carbonate reservoirs which can be utilized for geothermal energy and hydrocarbon production.

Appendix A

The differential effective medium (DEM) theory and the self-consistent approximation (SCA) are used to calculate the effective bulk modulus and Poisson's ratio of heterogeneous rocks.

The coefficient P and Q used in Equations (1, 2, 3, 4) to calculate the effective young's modulus and Poisson's ratio depend on the inclusion shape and the inclusion aspect ratio. The equation used to calculate P and Q

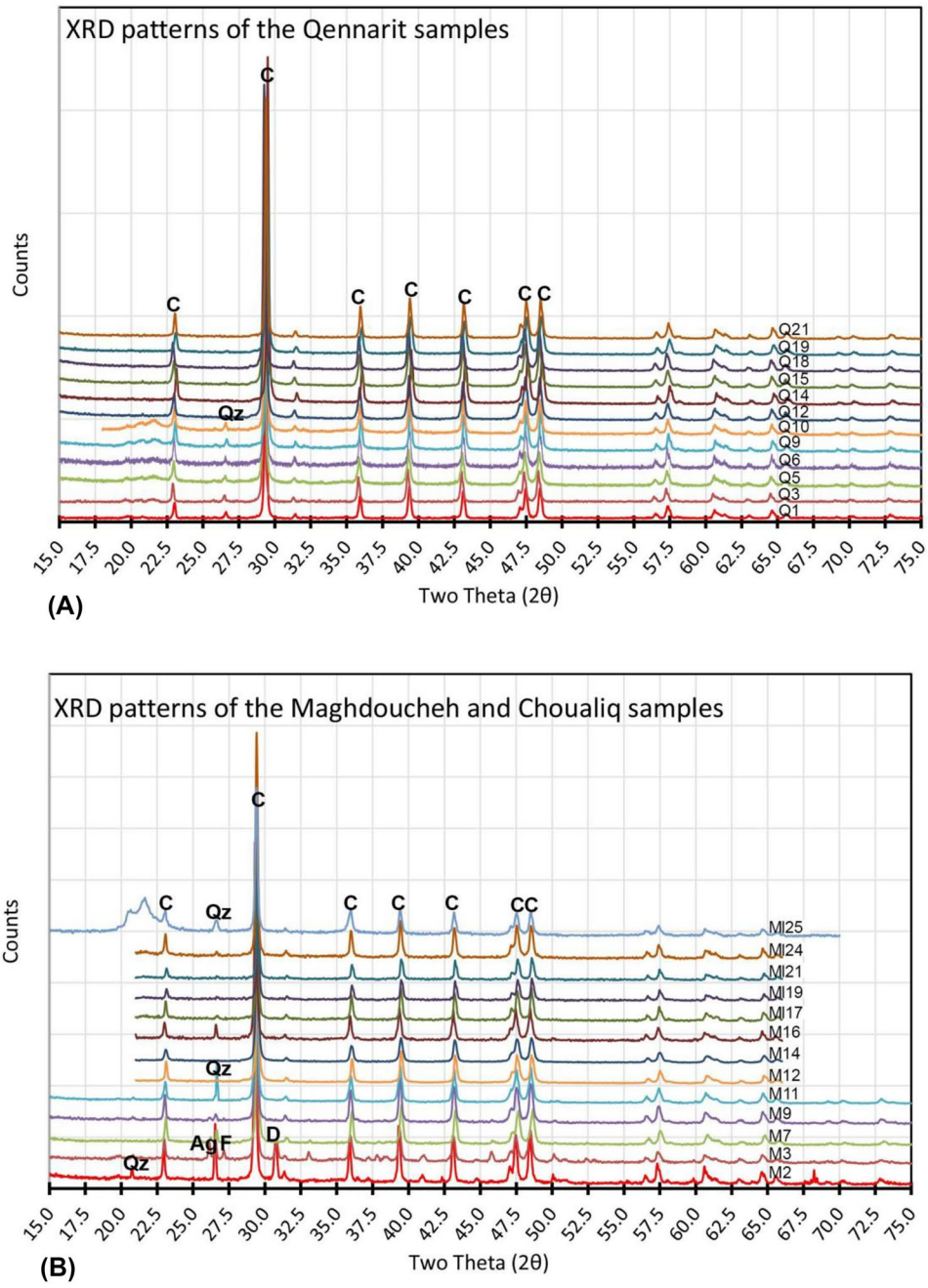

Fig. 12 XRD patterns of twenty-five samples from the studied sections. Symbols are as follows: C = calcite; Qz = quartz; D = dolomite; F = feldspar; Ag = aragonite

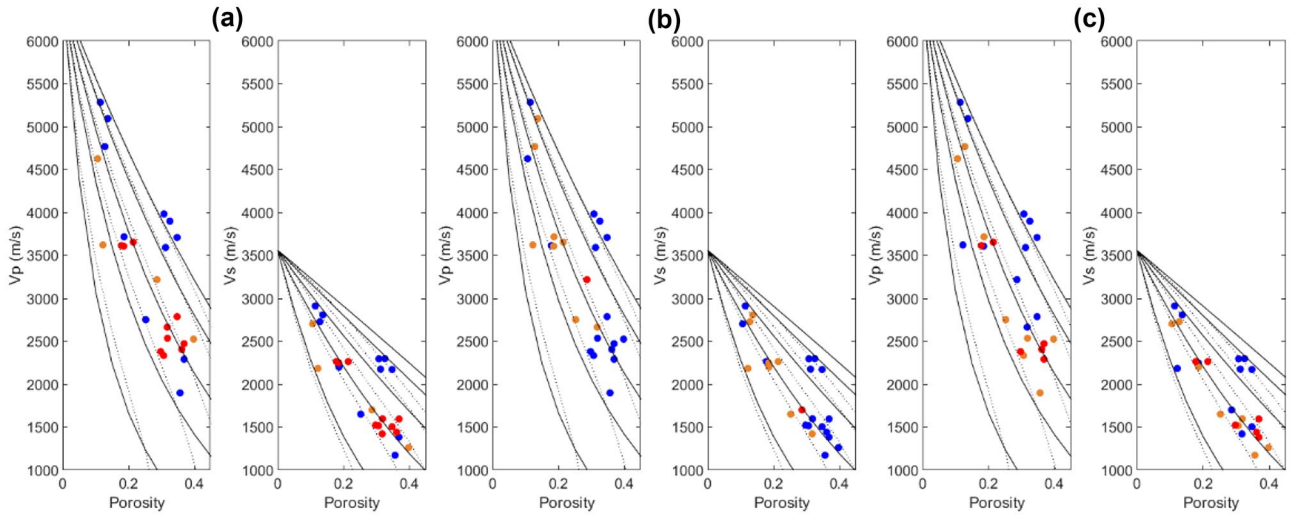

Fig. 13 Graphics showing the Vp and Vs as a function porosity with the data points classified based on the **a** microfacies, **b** pore types, and **c** insoluble residue fraction. Five dashed and five continuous lines correspond, respectively, to the SCA and DEM methods (with aspect ratios of 0.05, 0.08, 0.12, 0.17, and 0.2 from bottom to top in the case of the DEM method)

for a spherical, penny crack and ellipsoidal inclusions are detailed in A.1, A.2, and A.3, respectively (Mavko et al. 2009).

A.1 For a spherical inclusion

$$P = \frac{K_m + \frac{4}{3}\mu_m}{K_i + \frac{4}{3}\mu_m}$$

$$Q = \frac{\mu_m + \zeta_m}{\mu_i + \zeta_m}$$

where $\zeta = \frac{\mu}{6}\frac{(9K+8\mu)}{(K+2\mu)}$.

A.2 For a penny crack inclusion

$$P = \frac{K_m + \frac{4}{3}\mu_i}{K_i + \frac{4}{3}\mu_i + \pi\alpha\beta_m}$$

$$Q = \frac{1}{5}\left[1 + \frac{8\mu_m}{4\mu_i + \pi\alpha(\mu_m + 2\beta_m)} + 2\frac{K_i + \frac{2}{3}(\mu_i + \mu_m)}{K_i + \frac{4}{3}\mu_i + \pi\alpha\beta_m}\right]$$

where $\beta = \mu\frac{(3K+\mu)}{(3K+4\mu)}$ and α is the crack aspect ratio.

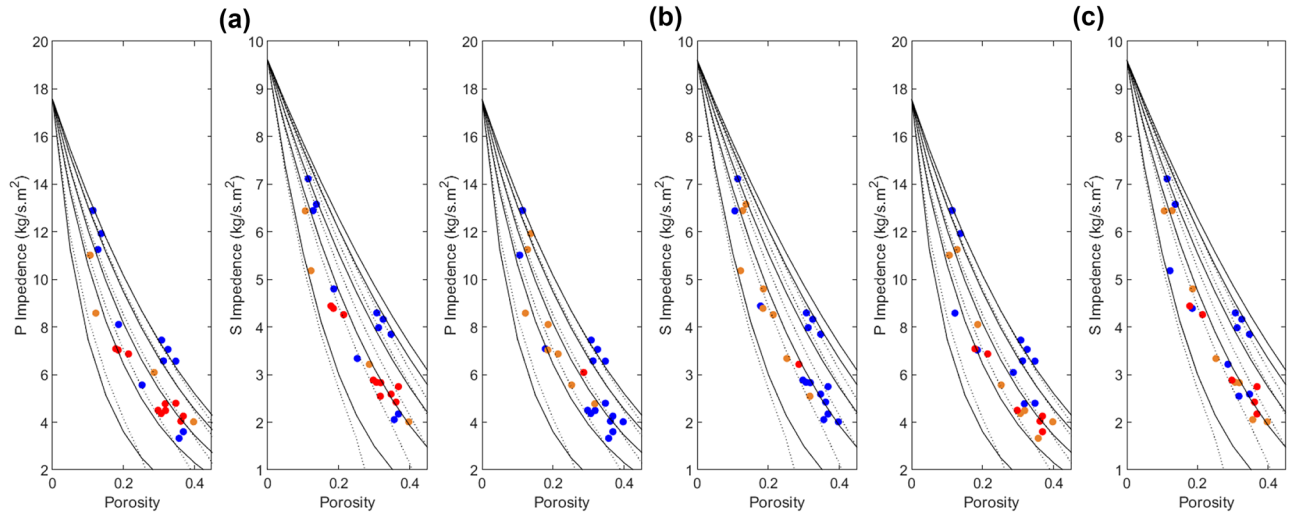

Fig. 14 Graphics showing the compressional and shear impedance as a function porosity with the data points classified based on the **a** microfacies, **b** pore types, and **c** insoluble residue fraction. Other details are similar to those of Fig. 13

A.3 For an ellipsoidal inclusion (Berryman 1980)

$$P = \frac{1}{3}T_{iijj}$$

$$Q = \frac{1}{5}(T_{ijij} - \frac{1}{3}T_{iijj})$$

where

$$T_{iijj} = 3\frac{F_1}{F_2}$$

$$T_{ijij} - \frac{1}{3}T_{iijj} = \frac{2}{F_3} + \frac{1}{F_4} + \frac{F_4F_5 + F_6F_7 - F_8F_9}{F_2F_4}$$

where

$$F_1 = 1 + A\left[\frac{3}{2}(f+\theta) - R\left(\frac{3}{2}f + \frac{5}{2}\theta - \frac{4}{3}\right)\right]$$

$$F_2 = 1 + A\left[1 + \frac{3}{2}(f+\theta) - \frac{1}{2}R(3f+5\theta)\right] + B(3-4R) + \frac{1}{2}A(A+3B)(3-4R)\left[f + \theta - R(f - \theta + 2\theta^2)\right]$$

$$F_3 = 1 + A\left[1 - \left(f + \frac{3}{2}\theta\right) + R(f+\theta)\right]$$

$$F_4 = 1 + \frac{1}{4}A\left[f + 3\theta - R(f-\theta)\right]$$

$$F_5 = A\left[-f + R\left(f + \theta - \frac{4}{3}\right)\right] + B\theta(3-4R)$$

$$F_6 = 1 + A\left[1 + f - R(f+\theta)\right] + B(1-\theta)(3-4R)$$

$$F_7 = 2 + \frac{1}{4}A\left[3f + 9\theta - R(3f+5\theta)\right] + B\theta(3-4R)$$

$$F_8 = A\left[1 - 2R + \frac{1}{2}f(R-1) + \frac{1}{2}\theta(5R-3)\right] + B(1-\theta)(3-4R)$$

$$F_9 = A\left[(R-1)f - R\theta\right] + B\theta(3-4R)$$

$$A = \frac{\mu_i}{\mu_m} - 1$$

$$B = \frac{1}{3}\left(\frac{K_i}{K_m} - \frac{\mu_i}{\mu_m}\right)$$

$$R = \frac{(1-2\nu_m)}{2(1-\nu_m)}$$

$$f = \frac{\alpha^2}{1-\alpha^2}(2\theta - 2)$$

$$\theta = \begin{cases} \frac{\alpha}{(\alpha^2-1)^{3/2}}\left[\alpha(\alpha^2-1)^{1/2} - \cosh^{-1}\alpha\right], \textit{for prolate spheroid i.e.}, \alpha > 1 \\ \frac{\alpha}{(1-\alpha^2)^{3/2}}\left[\cosh^{-1}\alpha - \alpha(1-\alpha^2)^{1/2}\right], \textit{for oblate spheroid i.e.}, \alpha < 1 \end{cases}$$

Acknowledgements The authors thank the Editor-in-Chief of the Bulletin of Engineering Geology and the Environment and two anonymous reviewers for their lengthy revisions and fruitful comments which greatly improved the manuscript.

Funding This study was funded by the URB of the American University of Beirut (Award # 103603; Project # 24687).

Data availability Data is available upon request from authors.

Declarations

Competing interests The authors declare no competing interests.

References

Abd El-Aal AK, Salah MK, Khalifa MA (2020) Acoustic and strength characterization of Upper Cretaceous dolostones from the Bahariya Oasis, Western Desert, Egypt: The impact of porosity and diagenesis. J Petrol Sci Eng 187:106798. https://doi.org/10.1016/j.petrol.2019.106798

Akbar M, Vissarpragada B, Alghamdi AH, Allen D, Herron M, Carnegie A, Dutta D, Olesen J-R, Chourasiya RD, Logan D, Steif D, Netherwood R, Russell SD, Saxena K (2001) A snapshot of carbonate reservoir evaluation. Oilfield Rev 12:20–41

Ali A, Wagreich M, Strasser M (2018) Depositional constraints and diagenetic pathways controlling petrophysics of Middle Miocene shallow-water carbonate reservoirs (Leitha limestones), Central Paratethys. Austria-Hungary Mar Petrol Geol 91:586–598

Alsuwaidi M, Mohamed AA, Mansurbeg H, Morad S, Alsuwaidi A, Al-Shalabi EW, Gomes J, Al-Ramadan K, Mohammed IQ, Farouk S (2021) Depositional and diagenetic controls on reservoir quality of microporous basinal lime mudstones (Aptian). United Arab Emirates Sed Geol 420:105925

Amel H, Jafarian A, Husinec A, Koeshidayatullah A, Swennen R (2015) Microfacies, depositional environment and diagenetic evolution controls on the reservoir quality of the Permian Upper Dalan Formation, Kish Gas Field, Zagros Basin. Mar Petrol Geol 67:57–71.

Anselmetti FS, Eberli GP (1993) Controls on sonic velocity in carbonates. Pure Appl Geophys 141(2–4):287–323

Anselmetti FS, Eberli GP (2001) Sonic velocity in carbonates - a combined product of depositional lithology and diagenetic alterations. In: Ginsburg R (Ed.), Subsurface geology of a prograding carbonate platform margin, Great Bahama Bank: Results of the Bahamas Drilling Project. SEPM Spec Publ 70:193–216

Babasafari AA, Bashir Y, Ghosh DP, Salim AMA, Janjuhah HT, Kazemeini SH, Kordi M (2020) A new approach to petroelastic modeling of carbonate rocks using an extended pore-space stiffness method, with application to a carbonate reservoir in central Luconia, Sarawak, Malaysia. Lead Edge 39(8):592a591–592a510

Berryman JG (1980) Long-wavelength propagation in composite elastic media. J Acoust Soc Am 68(6):1809–1831. https://doi.org/10.1121/1.385171

Blatt H (1992) Sedimentary petrology. W H Freeman & Company, New York, p 524

BouDagher-Fadel M, Clark GN (2006) Stratigraphy, paleoenvironment and paleogeography of Maritime Lebanon: a key to Eastern Mediterranean Cenozoic history. Stratigraphy 3(2):81–118

Brigaud B, Vincent B, Durlet C, Deconinck J-F, Blanc P, Trouiller A (2010) Acoustic properties of ancient shallow-marine carbonates: effects of depositional environments and diagenetic processes (Middle Jurassic, Paris Basin, France). J Sediment Res 80(9):791–807

Budd DA (2002) The relative roles of compaction and early cementation in the destruction of permeability in carbonate grainstones: a case study from the Paleogene of west-central Florida. USA J Sed Res 72(1):116–128

Busch B, Adelmann D, Herrmann R, Hilgers C (2022) Controls on compactional behavior and reservoir quality in a Triassic Buntsandstein reservoir, Upper Rhine Graben. SW Germany Mar Petrol Geol 136:105437

Brett CE, Brookfield ME (1984) Morphology, faunas and genesis of ordovician hardgrounds from Southern Ontario, Canada. Palaeogeogr. Palaeoclimatol. Palaeoecol 46:233–290

Choquette PW, Pray LC (1970) Geologic nomenclature and classification of porosity in sedimentary carbonates. AAPG Bull 54(2):207–250

Christensen NI, Szymanski DL (1991) Seismic properties and the origin of reflectivity from a classic Paleozoic sedimentary sequence, Valley and Ridge province, southern Appalachians. Geol Soc Am Bull 103:277–289

Croizé D, Ehrenberg SN, Bjørlykke K, Renard F, Jahren J (2010) Petrophysical properties of bioclastic platform carbonates: implications for porosity controls during burial. Mar Petrol Geol 27:1765–1774. https://doi.org/10.1016/j.marpetgeo.2009.11.008

Dubertret L (1945) Géologie du site de Beyrouth avec carte géologique au 1/20.000

Dubertret L (1955) Carte géologique du Liban au 1/200000 avec notice explicative. R_epublique Libanaise, Minist_ere desTravaux Publiques, *Beirut*, pp. 74

Dürrast H, Siegesmund S (1999) Correlation between rock fabrics and physical properties of carbonate reservoir rocks. Int J Earth Sci 88(3):392–408

Dvorkin J, Gutierrez MA, Grana D (2014) Seismic reflections of rock properties. Cambridge University Press, Cambridge

Eberli GP, Baechle GT, Anselmetti FS, Incze ML (2003) Factors controlling elastic properties in carbonate sediments and rocks. Lead Edge 22(7):654–660

Ehrenberg SN, Walderhaug O (2015) Preferential calcite cementation of macropores in microporous limestones. J Sed Res 85:780–793

Fallah-Bagtash R, Jafarian A, Husinec A, Adabi MH (2020) Diagenetic stabilization of the Upper Permian Dalan Formation, Persian Gulf Basin. J Asian Earth Sci 189:104144

Flügel E (2010) Practical use of microfacies: reservoir rocks and host rocks. Microfacies of Carbonate Rocks 877–894

Flügel E (2012) Microfacies analysis of limestones. Springer-Verlag, Berlin Heidelberg

Friedman GM (1964) Early diagenesis and lithification in carbonate sediments. J Sediment Res 34(4):777–813

Gardner G, Gardner L, Gregory A (1974) Formation velocity and density-the diagnostic basics for stratigraphic traps. Geophys 39:770–780

Ge Y, Lokier SW, Hoffmann R, Pederson CL, Neuser RD, Immenhauser A (2020) Composite micrite envelopes in the Lagoon of Abu Dhabi and their application for the recognition of ancient firm-to hardgrounds. Mar Geol 423:106141

Ghadami N, Rasaei MR, Hejri S, Sajedian A, Afsari K (2015) Consistent porosity–permeability modeling, reservoir rock typing and hydraulic flow unitization in a giant carbonate reservoir. J Petrol Sci Eng 131:58–69

Grundtner M-L, Gross D, Samsu A, Linzer H, Misch D, Sachsenhofer R, Scheucher L, Schnitzer S (2016) Diagenesis in Cenomanian clastic reservoir rocks of the Alpine Foreland Basin (Austria). In: 78th EAGE Conference and Exhibition 2016:1–5. https://doi.org/10.3997/2214-4609.201600702

Hajikazemi E, Al-Aasm I, Coniglio M (2010) Subaerial exposure and meteoric diagenesis of the Cenomanian-Turonian Upper Sarvak Formation, Southwestern Iran. Geol Soc London Spec Publ 330(1):253–272

Hashim MS, Kaczmarek SE (2019) A review of the nature and origin of limestone microporosity. Mar Petrol Geol 107:527–554

Hawie N, Deschamps R, Nader FH, Gorini C, Müller C, Desmares D, Hoteit A, Granjeon D, Montadert L, Baudin S (2014) Sedimentological and stratigraphic evolution of northern Lebanon since the Late Cretaceous: implications for the Levant margin and basin. Arab J Geosci 7:1323–1349. https://doi.org/10.1007/s12517-013-0914-5

Hussein AW, Abd El-Rahman Y (2020) Diagenetic evolution of the Eocene ramp carbonates (a Paradigm from the Nile Valley, Egypt): petrographical and geochemical attributes. Mar Petrol Geol 119:104484

Janjuhah HT, Alansari A (2020) Offshore carbonate facies characterization and reservoir quality of Miocene rocks in the southern margin of South China Sea. Acta Geologica Sinica-Eng Ed 94(5):1547–1561

Janjuhah HT, Alansari A, Santha PR (2019a) Interrelationship between facies association, diagenetic alteration and reservoir properties evolution in the Middle Miocene carbonate build up, Central Luconia, offshore Sarawak. Malaysia Arab J Sci Eng 44(1):341–356

Janjuhah HT, Alansari A, Vintaned JAG (2019b) Quantification of microporosity and its effect on permeability and acoustic velocity in Miocene carbonates, central Luconia, offshore Sarawak. Malaysia J Petrol Sci Eng 175:108–119

Janjuhah HT, Salim AMA, Alansari A, Ghosh DP (2018) Presence of microporosity in Miocene carbonate platform, Central Luconia, Offshore Sarawak. Malaysia Arab J Geosci 11(9):204

Janjuhah HT, Salim AMA, Ghosh DP, Wahid A (2017) Diagenetic processes and their effect on reservoir quality in Miocene carbonate reservoir, offshore, Sarawak, Malaysia. In: Icipeg 2016. Springer: pp: 545–558

Janjuhah HT, Sanjuan J, Alqudah M, Salah MK (2021) Biostratigraphy, depositional and diagenetic processes in carbonate rocks from southern Lebanon: impact on porosity and permeability. Acta Geologica Sinica-Eng Ed 95(5):1668–1683. https://doi.org/10.1111/1755-6724.14695

Jiang L (2022) Diagenesis of the San Andres Formation in the Seminole unit in Central Basin platform. West Texas AAPG Bull 106:267–287

Jiang L, Pan W, Cai C, Jia L, Pan L, Wang T, Li H, Chen S, Chen Y (2015) Fluid mixing induced by hydrothermal activity in the Ordovician carbonates in Tarim Basin, China. Geofluids 15:483–498. https://doi.org/10.1111/gfl.12125

Jiang L, Worden RH, Cai C (2014) Thermochemical sulfate reduction and fluid evolution of the Lower Triassic Feixianguan Formation sour gas reservoirs, northeast Sichuan Basin. China AAPG Bull 98:947–973. https://doi.org/10.1306/10171312220CorpusID:129056667

Jiang L, Worden R, Cai C et al (2018a) Contrasting diagenetic evolution patterns of platform margin dolostone and limestone in the Lower Triassic Feixianguan Formation, Sichuan Basin. China Mar Petrol Geol 92:332–351

Jiang L, Worden RH, Cai C, Shen A, Crowley SF (2018b) Diagenesis of an evaporite-related carbonate reservoir in deeply buried Cambrian strata, Tarim Basin. Northwest China AAPG Bull 102:77–102. https://doi.org/10.1306/0328171608517048

Jiang L, Worden R, Yang C (2018c) Thermochemical sulfate reduction can improve carbonate reservoir quality. Geochim Cosmochim Acta 223:127–140

Jin X, Dou Q, Hou J, Huang Q, Sun Y, Jiang Y, Li T, Sun P, Sullivan C, Adersokan H, Zhang Z (2017) Rock-physics-model-based pore type characterization and its implication for porosity and permeability qualification in a deeply-buried carbonate reservoir, Changxing formation, Lower Permian, Sichuan Basin. China J Petrol Sci Eng 153:223–233. https://doi.org/10.1016/j.petrol.2017.02.003

Jin Z, Liang T, Yi S, Wei K, Gao B, Shi L (2020) Depositional environment, diagenetic evolution, and their impact on the reservoir quality of the Carboniferous Kt-II Carbonate in the Zhanazhol Reservoir, Pre-Caspian Basin. Kazakhstan Mar Petrol Geol 117:104411

Jones SC (1972) A rapid accurate unsteady-state Klinkenberg permeameter. Soc Petrol Eng 383−397

Kearey P, Brooks M, Hill I (2002) An introduction to geophysical exploration. Blackwell Science Ltd., 3rd ed., 281 pp

Kenter JA, Podladchikov F, Reinders M, Van der Gaast SJ, Fouke BW, Sonnenfeld MD (1997) Parameters controlling sonic velocities in a mixed carbonate-siliciclastics Permian shelf-margin (upper San Andres formation, Last Chance Canyon, New Mexico). Geophys 62:505–520

Kerans C (1988) Karst-controlled reservoir heterogeneity in Ellenburger Group carbonates of west Texas: reply. AAPG Bull 72:1160–1183

Kershaw S, Munnecke A, Jarochowska E, Young G (2021) Palaeozoic stromatoporoid diagenesis: a synthesis. Facies 67(3):1–43

Kleipool L, Reijmer J, Badenas B, Aurell M (2015) Variations in petrophysical properties along a mixed siliciclastic carbonate ramp (Upper Jurassic, Ricla, NE Spain). Mar Petrol Geol 68:158–177

Lambert L, Durlet C, Loreau J-P, Marnier G (2006) Burial dissolution of micrite in Middle East carbonate reservoirs (Jurassic–Cretaceous): keys for recognition and timing. J Mar Petrol Geol 23(1):79–92

Loucks RG (1999) Paleocave carbonate reservoirs: origins, burial-depth modifications, spatial complexity, and reservoir implications. AAPG Bull 83:1795–1834

Loucks RG (2001) Modern analogs for paleocave-sediment fills and their importance in identifying paleocave reservoirs. Trans Gulf Coast Assoc Geol Soc 195−206

Martínez-Martínez J, Benavente D, García-del-Cura MA (2012) Comparison of the static and dynamic elastic modulus in carbonate rocks. Bull Eng Geol Env 71(2):263–268

Martini E (1970) Standard Paleogene calcareous nannoplankton zonation. Nature 226:560–561

Mavko G, Mukerji T, Dvorkin J (2009) The rock physics handbook: tools for seismic analysis of porous media, 2nd edn. Cambridge University Press, Cambridge

Morad D, Paganoni M, Al Harthi A, Morad S, Ceriani A, Mansurbeg H, Al Suwaidi A, Al-Aasm IS, Ehrenberg SN (2018) Origin and evolution of microporosity in packstones and grainstones in a Lower Cretaceous carbonate reservoir, United Arab Emirates. Geol Soc London Spec Publ 435(1):47–66

Müller C, Higazi F, Hamdan W, Mroueh M (2010) Revised stratigraphy of the Upper Cretaceous and Cenozoic series of Lebanon based on nannofossils. Geol Soc London Spec Publ 341(1):287–303

Neto IAL, Misságia RM, Ceia MA, Archilha NL, Oliveira LC (2014) Carbonate pore system evaluation using the velocity-porosity-pressure relationship, digital image analysis, and differential effective medium theory. J Appl Geophys 110:23–33. https://doi.org/10.1016/j.jappgeo.2014.08.013

Nurmi R, Standen E (1997) Carbonates, the inside story. Middle East Well Eval Rev 18:28–41

Oluwadebi AG, Taylor KG, Dowey PJ (2018) Diagenetic controls on the reservoir quality of the tight gas Collyhurst Sandstone Formation, Lower Permian, East Irish Sea Basin, United Kingdom. Sediment Geol 371:55–74

Paganoni M, Al Harthi A, Morad D, Morad S, Ceriani A, Mansurbeg H, Al Suwaidi A, Al-Aasm IS, Ehrenberg SN, Sirat M (2016) Impact of stylolitization on diagenesis of a Lower Cretaceous carbonate reservoir from a giant oilfield, Abu Dhabi, United Arab Emirates. Sediment Geol 335:70–92

Pei L, Blöcher G, Milsch H, Zimmermann G, Sass I, Li X, Huenges E (2020) Response of Upper Jurassic (Malm) limestone to temperature change: experimental results on rock deformation and permeability. Rock Mech Rock Eng 1−22

Raymer L, Hunt E, Gardner JS (1980) An improved sonic transit time-to-porosity transform. In: SPWLA 21st Annual Logging Symposium. Soc Petrophysicists and Well-Log Analysts

Regnet J, David C, Robion P, Menéndez B (2019) Microstructures and physical properties in carbonate rocks: a comprehensive review. Mar Petrol Geol 103:366–376

Regnet J, Robion P, David C, Fortin J, Brigaud B, Yven B (2015) Acoustic and reservoir properties of microporous carbonate rocks: implication of micrite particle size and morphology. J Geophys Res Solid Earth 120(2):790–811

Rosales I, Pérez-Garcia A (2010) Porosity development, diagenesis and basin modelling of a Lower Cretaceous (Albian) carbonate platform from Northern Spain. Geol Soc London Spec Publ 329(1):317–342

Salah MK, Alqudah M, Abd El-Aal AK, Barnes C (2018) Effects of porosity and composition on seismic wave velocities and elastic moduli of Lower Cretaceous rocks, central Lebanon. Acta Geophys 66:867–894. https://doi.org/10.1007/s11600-018-0187-1

Salah MK, Alqudah M, David Ch (2020a) Acoustics and petrophysical investigations on upper cretaceous carbonate rocks from northern Lebanon. J Afr Earth Sci 172:103955. https://doi.org/10.1016/j.jafrearsci.2020a.103955

Salah MK, Alqudah M, David Ch (2020c) Petrophysical and acoustic assessment of carbonate rocks, Zahle area, central Lebanon. Bull Eng Geol Env 79:5455–5475. https://doi.org/10.1007/s10064-020-01900-0

Salah MK, Alqudah M, Monzer AJ, David Ch (2020b) Petrophysical and acoustic characteristics of Jurassic and Cretaceous rocks from central Lebanon. Carbonates Evaporites 35:12. https://doi.org/10.1007/s13146-019-00536-w

Salah MK, Janjuhah HT, Sanjuan J (2023) Analysis and characterization of pore system and grain sizes of carbonate rocks from southern Lebanon. J Earth Sci. https://doi.org/10.1007/s12583-020-1057-8

Salih M, Reijmer JG, El-Husseiny A (2020) Diagenetic controls on the elastic velocity of the early Triassic Upper Khartam Member (Khuff Formation, central Saudi Arabia). Mar Petrol Geol. https://doi.org/10.1016/j.marpetgeo.2020.104823

Soete J, Kleipool LM, Claes H, Hamaekers H, Kele S, Özkul M, Foubert A, Reijmer JJG, Swennen R (2015) Acoustic properties in travertines and their relation to porosity and pore types. Mar Petrol Geol 59:320–335. https://doi.org/10.1016/j.marpetgeo.2014.09.004

Sun YF, Berteussen K, Vega S, Eberli GP, Baechle GT, Weger RJ, Massaferro JL, Bracco Gartner GL, Wagner PD (2006) Effects of pore structure on 4D seismic signals in carbonate reservoirs. SEG Tech Program Expand Abstr 3260–3264. https://doi.org/10.1190/1.2370208

Swei G, Tucker ME (2012) Impact of diagenesis on reservoir quality in ramp carbonates: Gialo Formation (Middle Eocene), Sirt Basin. Libya J Petrol Geol 35(1):25–47

Telford WM, Geldart LP, Sheriff RE (1990) Applied geophysics, 2nd edn. Press, Cambridge Univ. https://doi.org/10.1017/CBO9781139167932

Thompson DL, Stilwell JD, Hall M (2015) Lacustrine carbonate reservoirs from early Cretaceous rift lakes of western Gondwana: pre-salt coquinas of Brazil and West Africa. Gondwana Res 28:26–51. https://doi.org/10.1016/j.gr.2014.12.005

Tomašových A, Gallmetzer I, Haselmair A, Zuschin M (2022) Inferring time averaging and hiatus durations in the stratigraphic record of high-frequency depositional sequences. Sedimentol 69:1083–1118. https://doi.org/10.1111/sed.12936

Tucker ME, Wright VP (2009) Carbonate Sedimentology. John Wiley & Sons

Van Smeerdijk Hood A, Wallace MW (2012) Synsedimentary diagenesis in a cryogenian reef complex: ubiquitous marine dolomite precipitation. Sediment Geol 255:56–71

Varkouhi S, Jaques Ribeiro LM (2021) Bimineralic middle Triassic ooids from Hydra Island: Diagenetic pathways and implications for ancient seawater geochemistry. The Depositional Record 7(2):344–369

Verwer K, Braaksma H, Kenter JAM (2008) Acoustic properties of carbonates: effects of rock texture and implications for fluid substitution. Geophys 73(2):B51–B65

Walley CD (1998) Some outstanding issues in the geology of Lebanon and their importance in the tectonic evolution of the Levantine region. Tectonophysics 145:63–72

Wang Z, Hirsche WK, Sedgwick G (1991) Seismic velocities in carbonate rocks. Can Pet Tech 30:112–122

Weger RJ, Eberli GP, Baechle GT, Massaferro JL, Sun Y-F (2009) Quantification of pore structure and its effect on sonic velocity and permeability in carbonates. AAPG Bull 93:1297–1317

Wenzhi Z, Suyun H, Wei L, Tongshan W, Youngxin L (2014) Petroleum geological features and exploration prospect of deep marine carbonate rocks in China onshore: a further discussion. Nat Gas Ind B I. https://doi.org/10.1016/j.ngib.2014.10.002

Wyllie M, Gregory A, Gardner G (1958) An experimental investigation of factors affecting elastic wave velocities in porous media. Geophys 23:459–493

Xi K, Cao Y, Jahren J, Zhu R, Bjørlykke K, Haile BG, Zheng L, Hellevang H (2015) Diagenesis and reservoir quality of the Lower Cretaceous Quantou Formation tight sandstones in the southern Songliao Basin. China Sediment Geol 330:90–107. https://doi.org/10.1016/j.sedgeo.2015.10.007

Zolotukhin AB, Ursin J-R (2000) Introduction to petroleum reservoir engineering. Høyskoleforlaget AS - Norwegian Academic Press, Kristiansand, p 402